NTNU

Norwegian University of
Science and Technology

A TEM Study of Boron-implanted Cubic Silicon Carbide, for Solar Cell Applications

Sigurd Slettemark Hovden

Preface

This master thesis is part of the research project *SunSiC*, which is a collaboration between SINTEF, the University of Oslo (UiO), Linköping University (LiU) and Saint Gobain. The aim of *SunSiC* is to show that cubic silicon carbide can be used as a material for a highly efficient intermediate band solar cell. *SunSiC* was initiated by SINTEF senior scientist Ole Martin Løvvik.

The experimental work performed in this master thesis has been carried out at Forskningsparken, where the utilised instruments are located.

Oslo, 20.05.2016

Sigurd Slettemark Hovden

Abstract

Recent research suggests that high doses of boron implantation can introduce an intermediate electron energy band in cubic silicon carbide (3C-SiC). This makes it a viable material for a highly efficient intermediate band solar cell. Implantation techniques do often introduce material defects which are unwanted in solar cells, as they generally act to increase charge carrier recombination, lowering the solar cell efficiency. Transmission electron microscopy has in this thesis been utilised to investigate the structural effects of boron implantation and subsequent annealing, which was found necessary for post-implantation recrystallisation. It was found that as-grown 3C-SiC from the University of Linköping is almost defect-free, disregarding macro scale domain phase boundaries. Boron implantation of 2-3 at% at 400°C was found to amorphise the 3C-SiC, and subsequent annealing at 1400°C for one hour was found to give complete recrystallisation. The boron implanted 3C-SiC does regain single crystallinity from the annealing procedure, but with a significant increase in stacking faults, as well as the formation of boron-rich precipitate phases. Electron diffraction data suggests some degree of boron substitution of silicon in the 3C-SiC lattice. An attempt to further investigate the nature of the boron distribution was performed using electron energy loss spectroscopy simulations and experiments, but was not successful. A method for simulating such spectra for 3C-SiC was however developed, and was found to give reliable results. The work performed in this thesis suggests that the boron implantation dose should be lowered to avoid precipitates and possibly also to avoid the formation of stacking faults. It is also suggested that the implantation temperature should be increased. This could possibly counteract amorphisation, removing the need for post-implantation annealing, and thus also avoid the formation of boron rich precipitates without lowering the boron implantation dose.

Sammendrag

Studier tyder på at høye doser bor-implantasjon kan introdusere et mellomliggende elektronbånd i kubisk silisiumkarbid (3C-SiC). Dermed kan materialet potensielt brukes i en høyeffektiv mellombånd-solcelle. Implantasjonsteknikker introduserer imidlertid ofte materialdefekter, og disse er uønsket i solcellematerialer. Dette er fordi de ofte øker rekombinasjon av ladningsbærere i materialet, og dermed senker solcellens effektivitet. Transmisjon elektronmikroskopi er i denne avhandlingen blitt brukt til å undersøke strukturelle effekter av bor-implantasjon og annilering. Annilering ble funnet nødvendig for rekrystallisering av implantert materiale. Avhandlingen viser at 3C-SiC fra Universitetet i Linköping er nærmest defektfritt, med unntak av domenegrenser på makroskala. Det er vist at 2-3 at% bor-implantasjon ved 400°C amorfiserer den kubiske silisiumkarbiden, og at en times annilering ved 1400°C fører til fullstendig rekrystallisasjon. Det annilerte materialet er monokrystallinsk, men viser en tydelig økning i stablefeil, i tillegg til utfelling av presipitatfaser med høyt borinnhold. Elektrondiffraksjonsdata tyder på bor-substitusjon av silisium i 3C-SiC-gitteret. Et forsøk på å undersøke bor-fordelingen ytterligere ble gjort med elektrontapsspektroskopi-simuleringer og -eksperimenter. Dette viste seg ikke å gi resultater. En metode for simulering av elektrontapsspektere i 3C-SiC ble imidlertid utviklet, og gav pålitelige resultater. Arbeidet i denne avhandlingen viser at bor-implantasjonsdosen bør senkes for å unngå presipitater, og muligens også for å unngå stablefeil. Det er også foreslått å øke implantasjonstemperaturen, noe som kan motvirke amorfisering. I så tilfelle vil man ikke lenger ha behov for annilering, og dermed unngå utfelling av presipitater uten å senke bor-implantasjonsdosen.

Contents

Chapter 1

Introduction

1.1 Background

The global electricity production is largely dependent on fossil fuels. Renewable electricity is as of 2015 estimated to represent 22.8 % [1] of total production, as shown in Figure 1.1. This is not sustainable in the long term, and there is thus need for more renewable electricity. Photovoltaics (PV) deliver renewable electricity by the conversion of photons from the sun into an electrical direct current. The technology dominating the PV market today is the silicon solar cell, and its efficiency has been improving steadily for the last 40 years [2]. The work to improve the silicon solar cell has in fact been so successful that the technology is approaching the theoretical maximum efficiency limit of 29 %, albeit under laboratory conditions [3, p. 36] [4].

It is desirable to achieve even higher efficiency for PV devices. This might be possible by using a semiconducting material with an intermediate electron energy band of suitable characteristics. An intermediate band solar cell (IBSC) would allow for more efficient absorption of the solar spectrum than what is achieved today by a traditional silicon solar cell. The development of such an intermediate band material is the aim of SINTEF's research
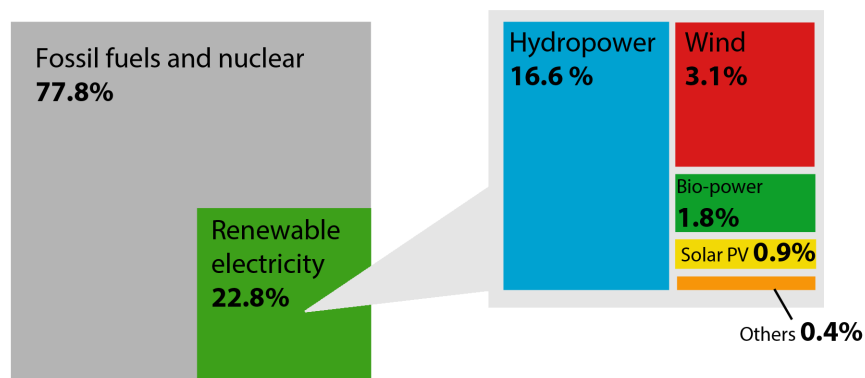

Figure 1.1: The estimated renewable share of global electricity production, 2015. Data from [1]

project *SunSiC*, which uses cubic silicon carbide (3C-SiC) as the semiconducting material. The intermediate electron band is to arise from implanting boron into the 3C-SiC at high concentrations. Growth of high quality 3C-SiC single crystals has for the first time been achieved by M. Syväjärvi, et al. at LiU [5]. They produce samples for *SunSiC*, and thus also this master thesis.

The materials characterisation in this master thesis has been performed using a Jeol 2100F, which is a transmission electron microscope (TEM). The TEM is fitted with several detectors, two of which were used in this thesis:

- Gatan Orius SC 1000W, a charge-coupled device (CCD) camera

- Gatan GIF 963; a post-column electron energy loss spectroscopy (EELS) detector

Computer simulations of electron energy loss (EEL) spectra have been performed using the real-space multiple-scattering code *Feff* [6] on the Abel supercluster at UiO.

1.2 Objectives and experimental approach

The main goal of this master thesis is to gain knowledge of how boron implantation and subsequent heat treatment (annealing) affects the atomic scale structure of 3C-SiC. The nature of the boron distribution in the 3C-SiC lattice is also a point of interest. The investigation is performed through the following objectives:

1. To make the TEM samples from:

    - Pure 3C-SiC
    - Boron implanted 3C-SiC
    - Annealed, boron implanted 3C-SiC

2. To obtain and analyse atomic resolution images

3. To obtain and analyse diffraction patterns

4. To simulate EEL spectra

5. To obtain experimental EEL spectra, and analyse them together with simulations.

The atomic resolution images are used for observing changes in the defect density between samples, in addition to other directly observable changes to the 3C-SiC lattice with boron implantation. Diffraction patterns as well as EELS simulations and experiments are used for testing hypotheses relating to the nature of boron distribution.

1.3   Limitations

As always will be the case for transmission electron microscopy, it is difficult to know whether what you see in the microscope is representative for the bulk sample or not. Sample preparation may introduce defects and artefacts into the TEM sample. This has been kept in mind, and care has been taken during sample preparation to minimise mechanical damage and contamination. The sample volumes investigated in a TEM are very small, as desired sample thicknesses typically are 100 nm (1 nm = 10^{-9} meters) or less. This is a limitation if one wants to extrapolate bulk material characteristics from TEM sample characterisation.

Limitations to specific experimental data are treated individually in Chapter 5.

1.4   Structure of the thesis

A general introduction to photovoltaics and the IBSC concept is firstly given in Chapter 2. The *deep level impurity*-approach is discussed further, before a literature survey of developments in that field. Chapter 3 treats selected silicon carbide structures, in addition to crystal growth. The breakthroughs in crystal growth of the cubic polytype at LiU during recent years are explained to provide a background for understanding the samples investigated in this thesis. The experimental methods, and selected theory relating to the experiments is given in Chapter 4. All experimental results are presented and discussed in Chapter 5. Chapter 6 concludes the thesis, and suggests future directions for the *SunSiC* project. A complete list of abbreviations and symbols are found in Appendix A. Additional data is given in Appendix B. All sources are listed at the very end.

Chapter 2

Intermediate band solar cells

The concept of the intermediate band solar cell was first published in 1997 by Luque and Martí [7]. They proposed that the efficiency of a photovoltaic (PV) device can be increased significantly by manipulating a semiconductor such that it obtains an intermediate electron energy band (IB) between the valence- and conduction band. The IBSC research is still in its infancy, and the developed prototype cells are so far drastically outperformed by the commercial silicon cells [2]. A simplified background on photovoltaics is given before the IBSC concept is explained further. A literature survey of developments in the IBSC research field with emphasis on the *deep level impurity* concludes the chapter.

2.1   Photovoltaics

The valence band (VB) and conduction band (CB) in a semiconductor span different electron energy ranges, and they are separated by a band-gap (E_g) of forbidden electron energies. The ground state of a semiconductor at zero kelvin is an empty CB and a VB of filled electron states. A photon can excite electrons across E_g if it has sufficient energy, as illustrated in Figure 2.1. A photon's energy depends on its wavelength as

$$E_{photon} = \frac{hc}{\lambda} \tag{2.1}$$

where h is Planck's constant ($4.1357 \cdot 10^{-15}$ eVs), c is the speed of light ($2.9979 \cdot 10^{8}$ m/s), and λ is the photon's wavelength [3, p. 8]. Photons with less energy than E_g are not absorbed by the semiconductor because there are no possible electron energy states within E_g. Photons with higher energy than E_g excite electrons higher up in the conduction band, and these high energy electrons quickly relax down to the conduction band edge. This happens through phonon interactions on the timescale of a few femtoseconds, with the result that their excess energy ($E_{excess} = E_{photon} - E_g$) is very quickly dissipated as heat in the material [3, p. 41, 309].

While electrons in the VB are bound to their corresponding atoms, electrons in the CB are free to move through the material, hence the name *conduction band*. When an electron is excited into the CB of a semiconductor, it leaves the absence of itself in the VB. This absence of a normally present electron is referred to as a hole, and it is associated with a
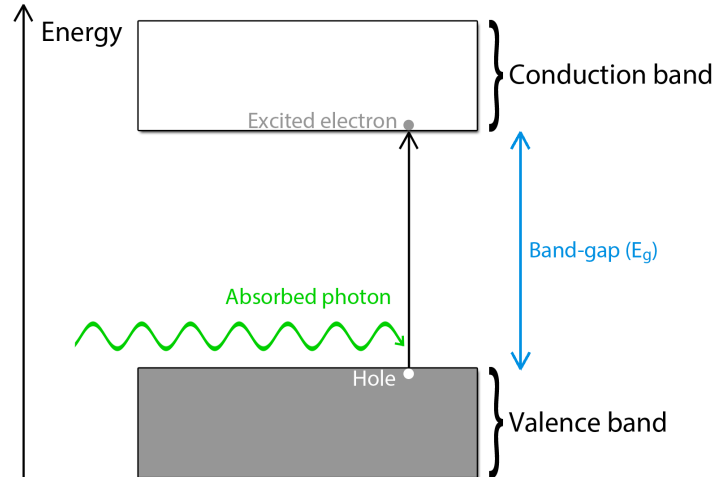
Figure 2.1: The photon-induced excitation of an electron from the filled valence band to the empty conduction band in a semiconductor.

positive unit of charge. Electrons and holes are often referred to as *charge carriers* or sometimes just *carriers*, since they carry charge. The hole in the VB is free to move throughout the material much like the electron is free to move while being in the excited state. The degree to which an electron and a hole is able to move in a particular material, is referred to *electron-* and *hole mobility* for that specific material [8, p.208]. Electron mobilities are in general higher than hole mobilities. The electron and the hole will inevitably recombine spontaneously within the material after an amount of time, emitting a photon in the process. This is referred to as *radiative recombination*, and the emitted photon has wavelength corresponding to E_g. This process is a fundamental counterpart to the absorption process, and is unavoidable in PV [9]. Other forms of recombination might also occur. These include Auger recombination and Shockley Read Hall (SRH) recombination, and fall under the category *non-radiative recombination* [3, p. 105-106], as these processes do not emit photons. The three recombination processes are illustrated in Figure 2.2. SRH recombination happens because of defects and/or impurities in the semiconductor. Defects and impurities often introduce localised electron energy states within E_g, where electrons and holes easily recombine [10]. *Localised* means spatially localised in the crystal. Auger recombination happens when an excited electron interacts with, and gives up its excitation energy, to another electron in the CB. This second electron then rapidly decays to the CB edge through phonon interactions, much like the electrons excited high up in the CB by high-energy photons mentioned earlier. All forms of recombination is unwanted in a PV device, as it acts to lower the device's efficiency. Non-radiative recombination is in principle avoidable in PV [9]. The time average before recombination happens determines the *carrier lifetime*. High carrier lifetimes are desired for PV, as one needs to physically separate the electrons and holes into different contacts leading to an external circuit for electricity production.

A PV device is designed as a p-n junction, i.e. it has an internal electrical field as the result of p- and n-doping [3, p.186]. Positive and negative charges are affected in opposite manners by electric fields. Electrons and holes are thus swept in different directions within
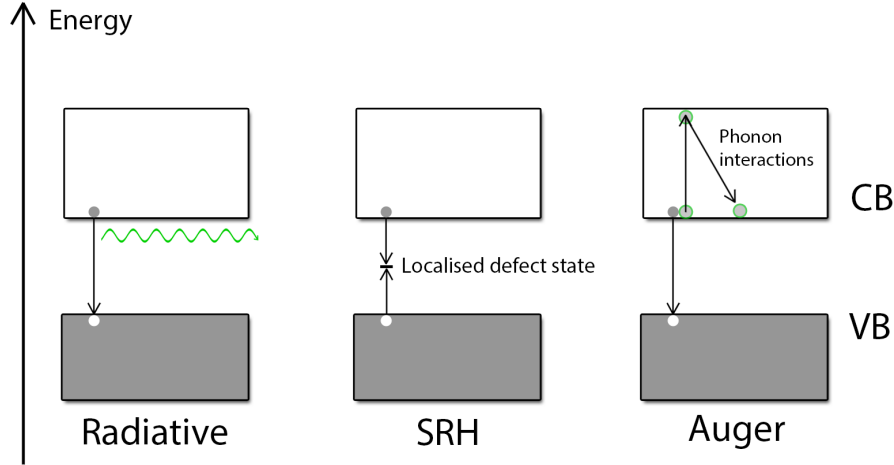
Figure 2.2: Radiative, SRH and Auger recombination. Auger recombination involves a second, already excited electron.

the p-n junction. In the ideal case, they are all swept into metal contacts before any of them recombine. The metal contacts lead to an external circuit, where the electrons and holes are exploited for electrical work. This is the working principle of PV devices (commonly called solar cells), admittedly rather simplified. An important point to note is that any photon with higher energy than E_g loses its E_{excess} as heat before it can be collected at the external circuit. There is in other words no extra gain from higher-than-E_g photons [3, p. 41, 309].

2.2 Exploitation of the solar spectrum

Electrical power is given by

$$P = VI \tag{2.2}$$

where I is the electric current passing through a voltage V [11, p. 44]. The open circuit voltage of a PV device under illumination is dependent on the magnitude of E_g with higher voltages for bigger band-gaps. The short circuit current is dependent on the amount of photons that are absorbed. The solar spectrum contains photons with a range of energies, so a bigger band-gap means fewer excited electrons and thus fewer electrons and holes to the external circuit. A PV material must therefore have a suitable E_g compared to the photon energies of the solar spectrum, since it is desirable that the highest possible amount of electrons are excited across a largest possible E_g. There exists in other words an optimum E_g for the most efficient exploitation of the solar spectrum by a single-band-gap PV device. This optimum E_g under one sun illumination, is calculated to be 1.35 eV, and gives a theoretical maximum efficiency of 33% at sea level [3, p. 33-34]. *One sun illumination* simply means un-concentrated light from the sun. The silicon solar cell has E_g of 1.11 eV [8, p. 188] which gives a theoretical maximum efficiency of 29% under one sun illumination [4]. This E_g corresponds to a photon wavelength of 1120 nm as calculated by Equation 2.1 and shown in Figure 2.3.
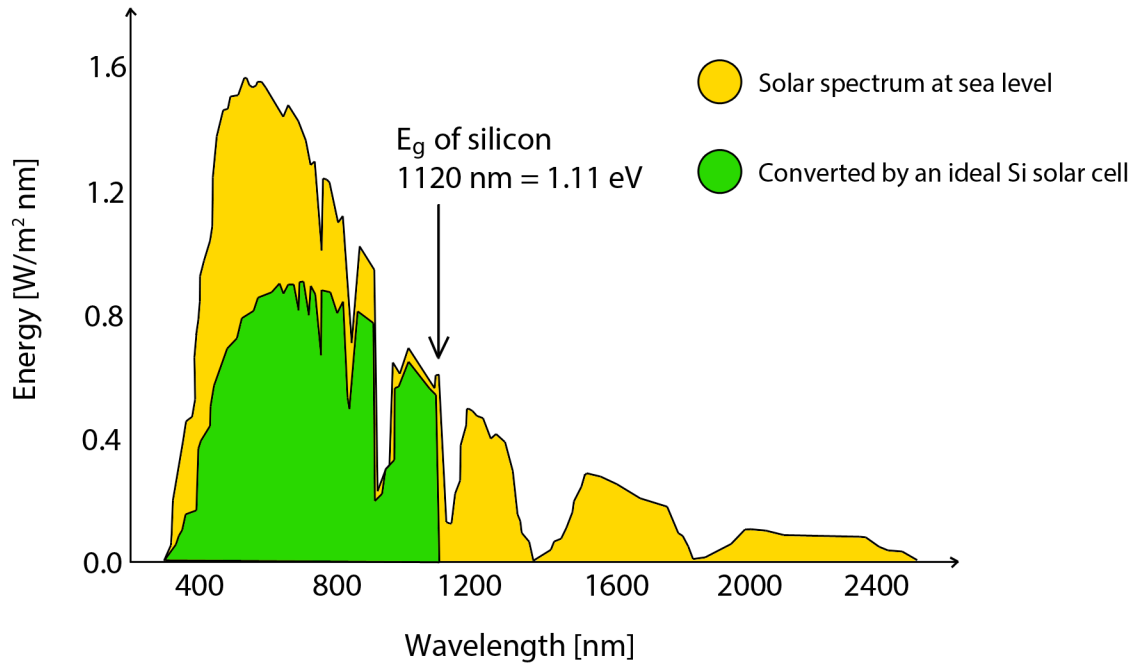
Figure 2.3: Schematic illustration of the solar spectrum at sea level, and the energy converted by an ideal Si solar cell. Figure based on data from [12].
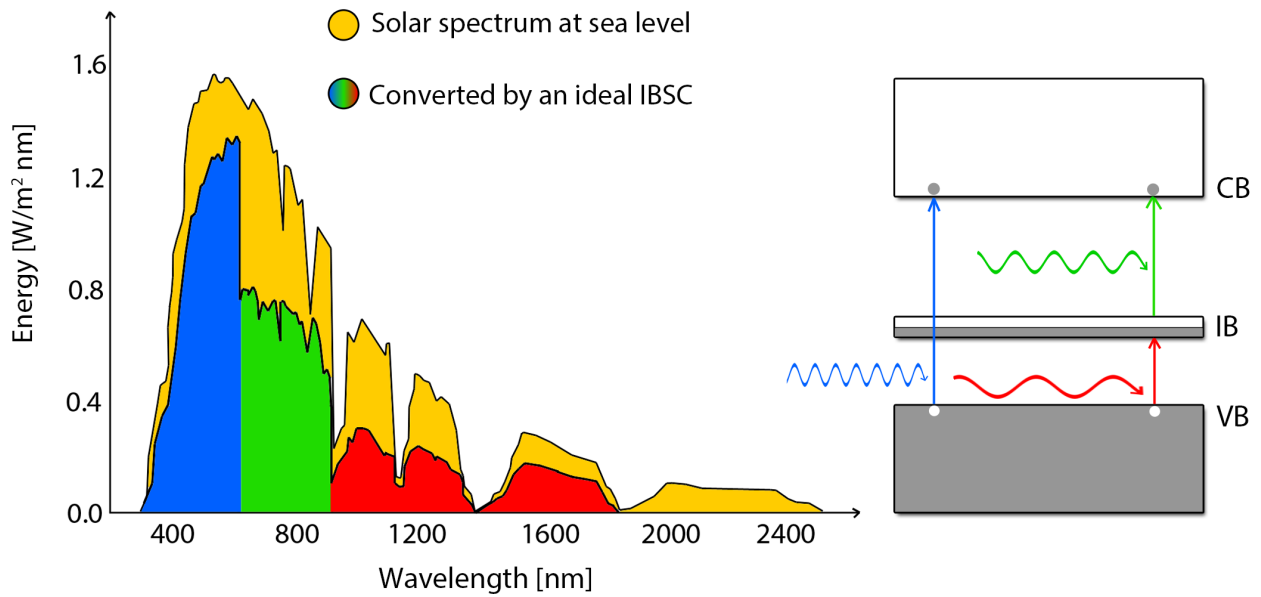

Figure 2.4: Schematic illustration of how the intermediate band allows for more efficient photo-absorption of the solar spectrum.

2.3 The intermediate band solar cell

With an intermediate band (IB) present within E_g, the solar spectrum can in theory be exploited more efficiently. The concept is illustrated in Figure 2.4. The intermediate band allows for three different excitation possibilities within the semiconductor; VB→IB, IB→CB and VB→CB. Photons of different energies may contribute to the promotion of electrons between different bands, and so more photons are absorbed in total. The optimal total E_g is larger for an IBSC than for a single-band-gap device. This results in a higher PV voltage with higher electron current and thus a higher power output in accordance with Equation 2.2. The theoretical maximum efficiency for a PV device with one intermediate electron energy band is calculated to be 46.8% under one sun illumination at sea level [13]. The total E_g is in the optimum case 1.97 eV, with the intermediate band located at either 0.71 eV above the VB or 0.71 eV below the CB [14]. For the best operating conditions under one sun illumination, the IB must be half filled at thermal equilibrium. When this is the case, there are always electrons in the IB available for excitation into the CB [15]. There have so far been three main approaches to achieve an IBSC:

- Quantum dot arrays

- Highly mismatched alloys

- Deep level impurities

the latter of which is further explored in this thesis. Most research has gone into quantum dot arrays, and in recent years, highly mismatched alloys [16]. There are, as of 2016, few articles on deep level impurity IBSCs in the literature, compared with the other two approaches. Impurities are in general associated with an increase in SRH recombination [10], which has probably made this approach seem unattractive.

2.4 The deep level impurity approach

The idea behind the deep level impurity approach is to introduce impurities into a semiconductor in high concentrations via some form of doping. IB theory predicts that wavefunctions of impurity atoms may delocalise (i.e. form a band) when added in sufficiently high concentrations [17]. Band formation is crucial because localised states increase SRH recombination [10]. *Deep level* as in *the deep level impurity approach* means that the introduced, delocalised energy level lies deep within E_g, rather than close to CB of VB. As mentioned earlier, the ideal IBSC has an intermediate band (delocalised electron energy levels) at 0.71 eV above VB or below CB. Rather high impurity concentrations are needed to form a band of delocalised states; typically more than 0.1 at%, depending on the material [18]. Luque and Martí, who came up with the IBSC concept in 1997 originally deemed it improbable that deep, delocalised states would form in a semiconductor as a result of doping or implantation [7]. However, computer simulations and recent research, both theoretical and experimental, show that this indeed is possible [19, 20, 21, 22].

The main challenge to overcome using this approach, is to establish the IB such that it

supports strong optical transitions while keeping the SRH recombination low. This is referred to as *lifetime recovery*. A 2012 theoretical study [23] claims that lifetime recovery cannot occur *".. because the metallic extended states will be localised by phonons during the recombination process"*. A highly effective deep level impurity IBSC is yet to be made, and SRH recombination might make it impossible. Research in the field is nevertheless ongoing.

2.4.1 Requirements for a potential deep level IBSC

A semiconductor for a potential deep level IBSC must have several characteristics. First of all, it must have a suitable E_g close to the ideal of 1.97 eV, and there must exist a way to introduce an intermediate band (delocalised states) at circa 0.71 eV away from CB or VB. The elements used should be cheap, easily available and not toxic nor rare. It must be possible and relatively cheap to manufacture high quality material at industrial scale. Single crystalline semiconductors with low defect concentrations are preferred because the presence of grain boundaries and defects may introduce localised electron energy states, and act as centres for recombination [10, 24]. The material should exhibit high electron- and hole mobility, and high carrier lifetimes. This makes the probability for charge collection at the cell contacts higher, and gives a better photocurrent yield. The material should be chemically and thermally stable over a wide range of conditions.

2.4.2 Deep level impurity research

This section is a literature survey of all experimental research concerning the introduction of a delocalised deep level impurity band in a semiconducting material, known to the author. The order is chronological with respect to when the research was done. The terms *doping* and *implantation* will be used somewhat interchangeably when referring to papers by other scientists. Implantation is a doping method, and it often implies high dopant concentrations, which is a requirement for the formation of delocalised states. Both *implantation* and *doping* refers to the introduction of a dopant (also called impurity element or foreign element) into a material.

2008: R. Lucena, et al. used density functional theory calculations to predict that In_2S_3 would obtain an IB when doped by Ti and V [20]. They synthesised the material and performed absorbance measurements. Evidence was found for an IB lying 0.5 eV above the VB within the 2 eV band-gap of the material. This study only includes materials characterisation; an IBSC prototype was not made.

2009: Wang, et al. found evidence for a deep level intermediate band in oxygen-doped ZnTe [21]. The group made an IBSC prototype. ZnTe has E_g of 2.26 eV, and the oxygen was found to introduce a level at 0.5 eV below the CB. Evidence for the intermediate band was found using photoluminescence measurements, and from the fact that oxygen doping increased the efficiency of the prototype. The device had only about 1% efficiency, but it was a proof of concept in that it showed a 50% increase in relative efficiency compared to the undoped cell [21].

2011: B. Marsen, et al. found sub-bandgap photoresponse in Fe-doped $CuGaS_2$ [25]. $CuGaS_2$ has E_g of 2.46 eV. The group made an IBSC prototype. They used absorbance measurements to achieve their data, and found increasing sub-bandgap absorption with increasing Fe doping at 1.2 and 1.9 eV. The SRH recombination did however also increase with Fe doping, suppressing the positive effect of sub-band-gap photoabsorbtion.

2013: P. G. Linares, et al. studied Ti-doped GaAs, and made an IBSC prototype [26]. GaAs has E_g of 1.42. Photo reflectance measurements were performed in the study. They found photoresponse from below-bandgap photons, but they struggled with poor crystal quality resulting from the doping procedure.

2013: J. Sheu, et al. measured photoresponses in an IBSC prototype made from Mn-doped GaN [27]. They used absorbance measurements to characterise the optical properties of their prototype. Their material had E_g of 3.4 eV, and they found evidence of a Mn impurity band at 1.5 eV above the VB. They conclude that their material "shows promising applications in IBSCs."

1976, 2003, 2014→: It was found in 1976 that boron form deep states at 0.74 eV above the VB in 3C-SiC [28]. B. Richards, et al. made an attempt in 2003 to use boron implanted 3C-SiC for increased carrier generation under illumination, but the study suffered from bad crystal quality [29]. M. Syväjärvi, et al. have in recent years achieved high quality 3C-SiC crystals [30, 5]. This has given *SunSiC* the opportunity to develop and research 3C-SiC as an IB material [31]. The group has performed photoluminescence measurements and absorbance measurements, and found evidence for optically active deep states at the predicted energy level. The results suggest IB formation. A boron implanted 3C-SiC prototype IBSC has not been made yet.

Several attempts on making a deep level impurity IB material have been presented, some of which included an IBSC prototype. None of the prototype's efficiencies can compare with the modern silicon solar cell. To optimise the efficiency of a potential IBSC, one should consider the E_g of the material. As stated in the section 2.4.1, the optimal E_g is at 1.97 eV with an intermediate band at 0.71 eV away from VB or CB. On that criterion, In_2S_3, ZnTe, $CuGaS_2$ and 3C-SiC are the most promising ones, as GaAs has a too-low E_g, and GaN a too-high one. Neither of CuGaS or SiC are made from too-expensive and rare materials, but the same is not true for ZnTe. This might cause the ZnTe to struggle commercially. The CuGaS cell had significant SRH recombination problems at the amounts of Fe doping required for IB formation. The authors of the CuGaS paper consider the research more a proof of concept than a potential IBSC. The SiC research does not involve an IBSC prototype, and it is in that sense not directly comparable to the CuGaS or ZnTe technology. The positive aspects of the potential 3C-SiC IBSC are among the following. It is made from very cheap and abundant elements, and it has several superior material characteristics. These are discussed in the next chapter. To confirm the presence of the intermediate band, a two-photon experiment must be performed for conclusive evidence according to A. Martí, et al. [32]. This has not been performed by the *SunSiC* project yet.

Chapter 3

Silicon carbide

Silicon carbide is a crystalline semiconductor compound with chemical formula SiC. It is a remarkably stable and hard material which was first fabricated for use as an abrasive in the late eighteen hundreds [33]. Due to its high chemical stability, it is commonly used in high temperature, high power and high radiation environments [34][35]. SiC also exhibit interesting functional properties as a semiconductor. The extraordinary combination of mechanical and electrical properties has made it an interesting material for study in recent years [36].

This chapter has two main parts. The first is about relevant SiC structures, the second about SiC crystal growth with emphasis on recent developments in the manufacture of high quality 3C-SiC crystals.

3.1   SiC structures

Atoms are arranged in a periodically repeating lattice in crystalline materials like SiC. There are many different ways to repetitively arrange silicon and carbon atoms in a lattice, giving the lattices different symmetries. This is referred to as *polymorphism*. SiC can crystallise with cubic, hexagonal and rhombohedral lattice symmetries. The stacking sequence of the close-packed atomic layer within the polymorph can vary. This is called *polytypism*. Figure 3.1 shows three common SiC polytypes; 3C-SiC, 4H-SiC and 6H-SiC. Purple dots are lattice points and not atoms, i.e. one Si atom *and* one C atom is associated with each dot. It might not be immediately apparent from the figure that the 3C structure is indeed cubic and not hexagonal. The close-packed layer in SiC has hexagonal symmetry for all polytypes, but the *unit cell* may still have non-hexagonal symmetry. A crystal's unit cell is the smallest group of atoms which has the overall symmetry of the crystal, and from which the entire lattice can be built, by repetition in three dimensions.

There are over 250 confirmed SiC polytypes [37], and so a precise naming system is needed to keep track of them. The most common polytypes are the ones in Figure 3.1 and are referred to as 3C, 4H and 6H [38]. The letter denotes lattice symmetry (cubic, hexagonal), and the number gives the stacking sequence's magnitude for the given polytype.
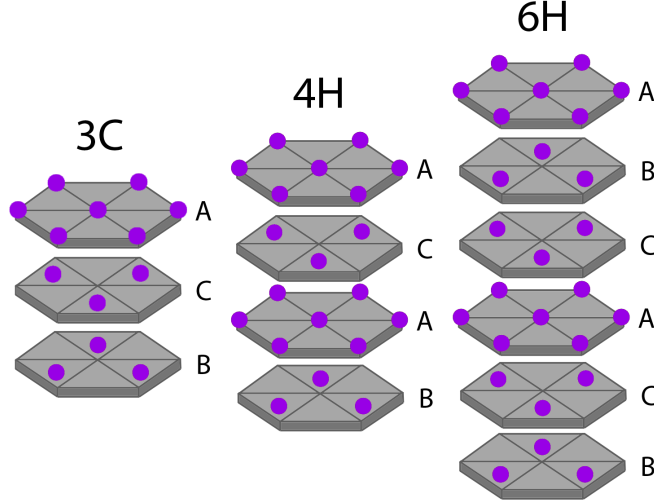
Figure 3.1: Stacking sequence of the close-packed planes in the three most common SiC polytypes. Purple dots are lattice points, and are associated with one Si atom and one C atom.

3.1.1   3C-SiC

3C-SiC is the only known cubic polytype of silicon carbide. It has a close-packed-layer period of three (ACB) and is described by the face-centered cubic Bravais lattice. With one carbon and one silicon atom associated with each lattice point, it belongs to the zincblende crystal system, space group F-43m. The unit cell is illustrated in Figure 3.2. The lattice parameter of the unit cell, a_{3C}, is 4.3591(2) Å [39]. 3C-SiC has an isotropic thermal expansion coefficient due to its cubic nature of $3.28 \cdot 10^{-6}$ K^{-1} [40]. Its band-gap is indirect and has has magnitude 2.36 eV [41]. The complete band diagram is given in the appendix, Figure B.1. The 3C-polytype has electron- and hole mobility of 1000 cm^2/Vs and 320 cm^2/Vs respectively [31]. Carrier lifetime of 8.2 μs in high quality 3C-SiC has been reported [42]. These latter electronic properties are among the reasons why the *SunSiC* project considers 3C-SiC as a good PV material, as the values are comparable with solar grade silicon [3, p. 185].

3.1.2   4H-SiC

4H-SiC is, as the name indicates, an hexagonal structure with a close-packed-layer period of four (ACAB). The 4H-SiC is described by space group P6$_3$mc. It has lattice parameters $a_{4H} = 3.07$ Å and $c_{4H} = 10.08$ Å [40]. Its unit cell is shown in Figure 3.2. As 4C-SiC is an hexagonal structure, its thermal expansion coefficient is non-isotropic, with magnitudes $3.30 \cdot 10^{-6}$ K^{-1} and $3.16 \cdot 10^{-6}$ K^{-1} for the a_{4H} and c_{4H} lattice parameters, respectively [40]. These are important parameters with regards to growth of 3C-SiC, as will be discussed. The band-gap of the 4H polytype is 3.23 eV, and is indirect in nature [41], as seen in Figure B.1.
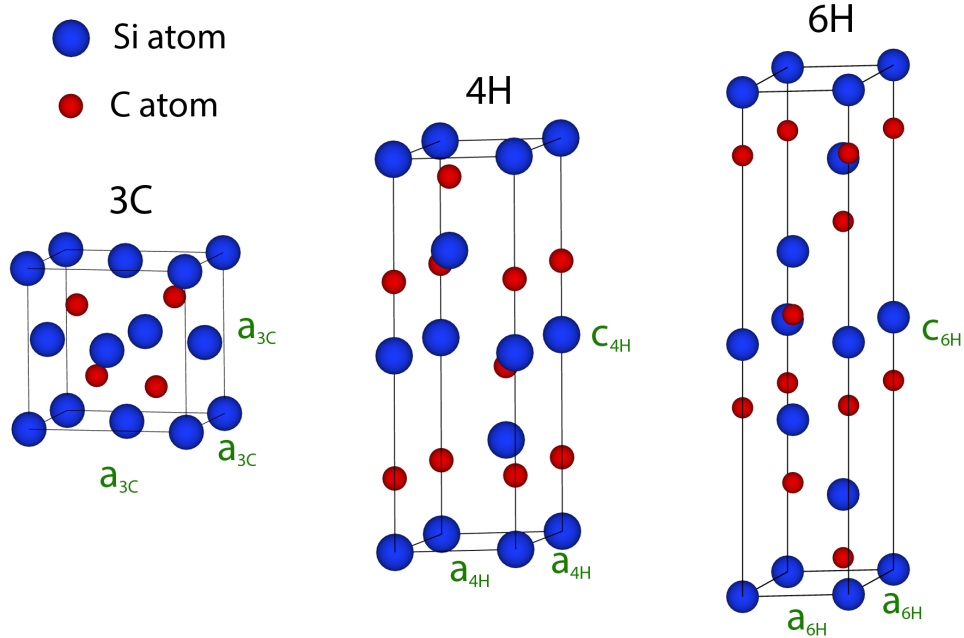
Figure 3.2: The unit cells of 3C-SiC, 4H-SiC and 6H-SiC. Letters a and c are lattice parameters with subscript reflecting the polytype.

3.1.3 6H-SiC

6H-SiC is the most common SiC polytype, and this polytype is generally implied when mentioning "silicon carbide" in scientific and daily language. It has a close-packed-layer period of six (ABCACB). The space group of 6H-SiC is the same as that of 4H-SiC, i.e. P6$_3$mc. Its unit cell is illustrated in Figure 3.2. The lattice parameters are a$_{6H}$ = 3.07 Å and c$_{6H}$ = 15.12 Å [40]. The band-gap is indirect with magnitude 3.0 eV, illustrated in Figure B.1.

3.2 Crystal growth

For electronic, and PV applications in particular, high crystal quality is crucial, as discussed in the previous chapter. This means few grains, preferably single crystals, high purity of the unimplanted crystal, and few lattice defects. For silicon this is achieved by the Czochralski process, where a large single crystal is pulled from a melt. This can not be achieved for SiC because it sublimes at all realistic pressures, regardless of polytype [43]. Methods for fabricating SiC crystals are among others liquid-phase epitaxy, chemical vapour deposition, and sublimation epitaxy, the latter of which is illustrated schematically in Figure 3.3. Sublimation epitaxy has been found to be the most successful growth technique for single crystals of SiC [43]. In this technique a SiC source powder is sublimed at elevated temperatures in a closed chamber. The vapour is transported via a temperature gradient (ΔT) to a substrate, where it condensates to form *adatoms*. When many adatoms adsorb on the substrate surface, they bind together and form a new crystal. One needs to control different parameters to achieve high quality crystal of desired composition and polytype. These parameters are nu-
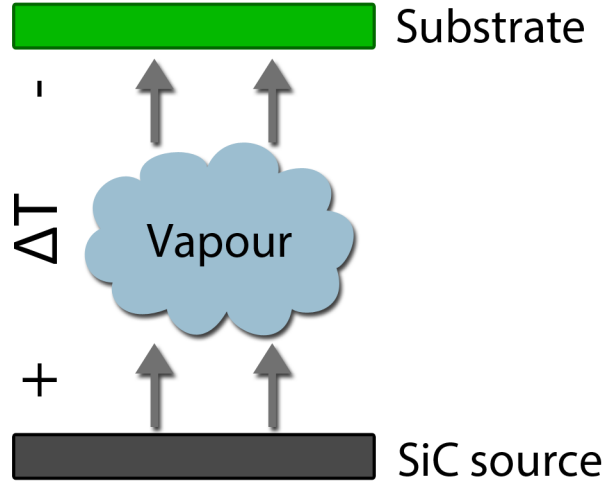
Figure 3.3: A schematic illustration of sublimation epitaxy

merous, and include the lattice parameter and thermal expansion coefficient of the substrate, in addition to temperature and pressure of the chamber, among others. The geometry of the setup also influences the crystal growth, as will become clear in the next few sections. The thickness of the grown material must be sufficient, so that the interface layer and substrate can be removed to get a free-standing grown crystal. This means that the growth technique must be relatively swift to be feasible for industrial upscale.

3.2.1 Progress in sublimation epitaxial growth of SiC

For sublimation epitaxy it is important to use a high quality substrate with matching lattice parameters and thermal expansion coefficient with respect to the crystal it is desired to grow. Matching parameters reduce the amount of interface induced defects, and is therefore crucial for a high quality grown crystal.

High quality single crystals of 6H-SiC have been successfully grown since the 1970s using a sublimation epitaxial method called the *Modified Lely Method* [44]. The Modified Lely Method uses SiC source powder, which is evaporated at temperatures exceeding 2200°C [45]. The vapour recrystallises on a seed wafer of single crystal 6H-SiC, which is maintained at a lower temperature. The cubic polytype has been more problematic to grow [35], since the Modified Lely Method can only produce 4H and 6H polytypes due to 3C's inferior stability at 2200°C and above [38]. The problems regarding growth of 3C-SiC are numerous, but the two main problems have been the following [30, 38]:

- Lack of suitable substrates

- Lack of high quality 3C seeds

Silicon substrates have been used for 3C growth due to their high crystal quality, but are not ideal because of a 20% lattice- and 8% thermal expansion coefficient mismatch. This results in a myriad of crystal defects, such as stacking faults, anti-phase boundaries and twins.
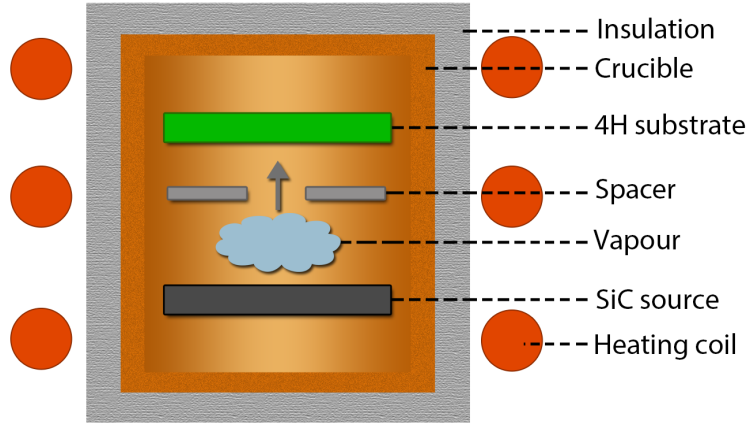
Figure 3.4: A schematic and simplified illustration of the 3C-SiC growth setup at LiU.

Hexagonal SiC polytypes have low lattice- thermal coefficient mismatch with 3C, and they should on that basis act as good substrates. They are also commercially available due to the Modified Lely method. However, there have been problems with the unintentional growth of substrate polytype instead of 3C as these are more stable at typical growth conditions [38]. The result is that 3C-SiC is not a well studied material to date due to the growth difficulties [43].

3.2.2 Growth of 3C-SiC at LiU

M. Syväjärvi's team at the University of Linköping have in recent years developed a novel growth technique based on sublimation epitaxy to obtain high quality single crystal 3C-SiC. They have overcome the substrate- and seed problem, and are for the first time able to achieve high quality crystals of 3C-SiC [5]. The crucible used in this sublimation epitaxial technique is illustrated schematically in Figure 3.4.

It has been found that 3C may nucleate on the (0001) plane of 4H and 6H-SiC at temperatures ranging from 1750-2000°C, using sublimation epitaxy [38]. However, the nucleation is hard to control. Nucleotides form randomly with different orientations at the whole substrate surface. A multi-crystalline, defect-rich 3C sample is then the result. To limit the area of which the nucleation may occur, Syväjärvi, et al. have found it advantageous to cut the substrate at an off-axis angle of 4° from the (0001) plane towards the $<11\bar{2}0>$ direction, as illustrated in Figure 3.5. This ensures preferential nucleation of a few 3C islands on the (0001)-terrace, and these islands grow to cover the whole substrate if the temperature is maintained. Such lateral extension on off-axis substrates is commonly referred to as *step-flow growth*. This setup is reported to result in few defects, apart from domain phase boundaries (DPBs) that result from the fact that multiple island may form on the terrace. To reduce the amount of initially nucleated islands on the terrace, geometrical control in form of a spacer is utilised as illustrated in Figure 3.6. At low growth temperatures, around 1800°C,
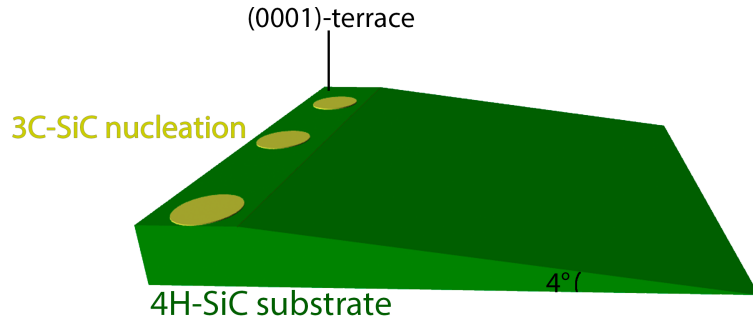
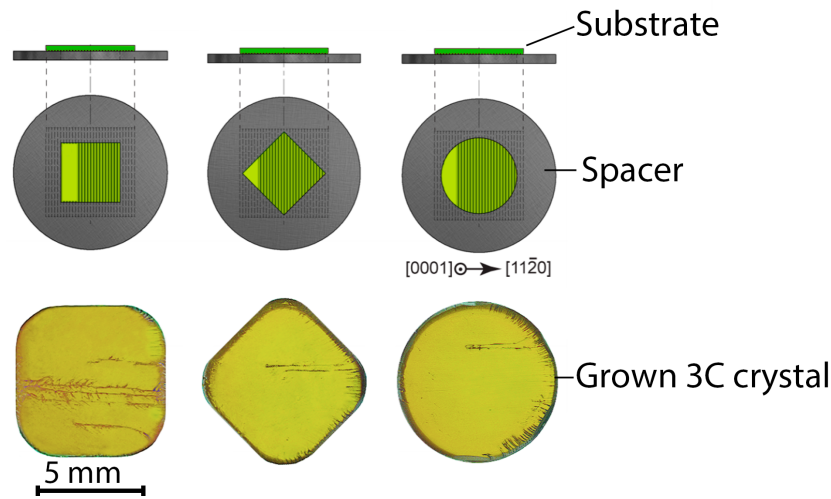Figure 3.5: The 4 degree off-axis geometry of the substrate

Figure 3.6: Schematic illustration of spacer geometry. The arrangements in the middle and right give fewer domains in the grown crystal. Figure modified from reference [5]

the number of DPBs is not reported to increase significantly during growth. However, this temperature makes the growth process too slow (100 µm/h thickness increase) for potential industrial upscale. A higher temperature gives faster growth, but considerably more defects. A two-step growth process has been found to reduce the growth time significantly without compromising crystal quality. The growth is initiated and maintained at 1800°C for 1 h to allow 3C to cover the substrate. The temperature is then increased to 1900°C, which gives a growth rate of 500 µm/h while still maintaining crystal quality. This temperature is maintained for 1 h 45 min to produce a 1 mm thick 3C crystal.

The LiU group has for the first time been able to produce high quality 3C-SiC crystals using this two step, geometrically controlled, off axis, step-flow sublimation epitaxy on a 4H substrate. However, they still face some challenges concerning the nucleation of parasitic 3C inclusions. These form spontaneously during growth, and give rise to DPBs. The LiU group suspects that this may be influenced by substrate quality [5].

Chapter 4

Experimental

This chapter explains the experimental techniques used for achieving the stated objectives. All experimental work is performed by the author, unless stated specifically otherwise. Selected theoretical background is given with regards to the different instruments and techniques utilised.

4.1 TEM sample preparation

The goal of TEM sample preparation is to achieve regions of electron-transparency in the sample. A thickness of maximum 50-100 nm is desired for electron energy loss spectroscopy (EELS) and atomic resolution images. The typical preparation procedure for a TEM sample has been the following.

The as-grown crystal, typically 6 mm by 6 mm, is cut into smaller pieces, approximately 3 mm by 3 mm, using a Technoorg Linda diamond disc cutter and/or a Rofin laser cutter. A cross section "sandwich" is made using 4H-SiC substrate material as support, glued together with Gatan Inc. epoxy, which hardens when heated. The sandwich is mounted on a pod for use in the Multiprep™ grinding and polishing system. The mounting adhesive used
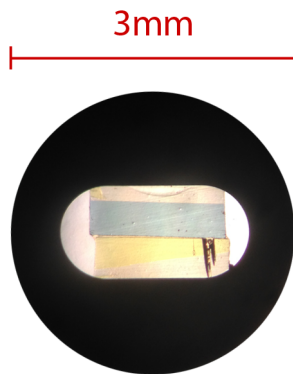

Figure 4.1: A typical TEM cross-section sample viewed in an optical microscope prior to ion milling. Yellow material is 3C-SiC. The copper slot appears black due to backlighting.

during grinding and polishing the first side of the sample, is Crystalbond™ which requires heating to liquify, and acetone to dissolve. The second side is ground and polished using a high precision pod, with Loctite Super Glue as adhesive. The sample is typically ground and polished down to approximately 20-30 µm. The diamond foils used in the Multiprep have grain sizes of 30, 15, 9, 6, 3, 1, 0.25 and 0.1 µm and are used in that respective order to minimise mechanical damage to the sample. The sample thickness is determined using optical microscopy. After grinding and polishing, regular time cured epoxy is used to attach the sample to a TEM copper slot. The sample and slot is then de-attached from the pod using acetone to dissolve the Loctite Super Glue. Samples are then cleaned using ethanol and tap water. Figure 4.1 shows the typical cross-section sample at this point. To achieve electron transparency, the sample is inserted into a Gatan PIPS II ion mill. The ion mill uses 0.1 - 4 keV argon ions to remove material from the sample until a hole is formed. Angles for the ion guns have been 8° for top gun and 7° for bottom gun. Liquid nitrogen cooling during ion milling has been utilised to reduce amorphisation of the TEM sample surface. Typical milling times are 2 hours at 4 keV, then approximately 2-30 minutes at 2-3 keV. After the formation of a hole in the sample, ion milling is ideally stopped immediately. Before TEM analysis, the samples have been plasma cleaned for 5 minutes in a Fishione plasma cleaner to remove surface contamination.

4.2 Transmission electron microscopy

4.2.1 Electrons as illumination

To investigate nature at the atomic level, one needs a powerful microscope. The theoretical resolving power of a visible light microscope (VLM) is given by

$$d = \frac{1.22\lambda}{NA_c + NA_o} \tag{4.1}$$

where d is the minimum resolved distance in nm, λ is the photon wavelength in nm, NA_c and NA_o are the numerical apertures of the condenser and objective lenses, respectively [46, p.87]. At best, this gives a resolving power of about 350 nm for green light. The VLM is thus useless if one wants to investigate structural features at the atomic scale, as typical atomic spacings in materials are on the order of ångströms (1 Å = 10^{-10} meters).

A transmission electron microscope is different from a VLM in that it uses electrons instead of photons to produce an image of the specimen. It is also different in that the waves (electrons in a TEM) transmit through the sample, hence the name *transmission* electron microscope. The use of electrons instead of light allows one to probe much smaller features, because the wavelengths of electrons are drastically shorter that those of photons. DeBroglie showed in the 1920s that the wavelength of an electron is related to its energy through

$$\lambda = \frac{1.22}{\sqrt{E}} \tag{4.2}$$

where E is the electron energy in eV, and gives the wavelength, λ, in nm. In a TEM one typically accelerate the electrons to 200 keV, which corresponds to a wavelength of 2.73 pm
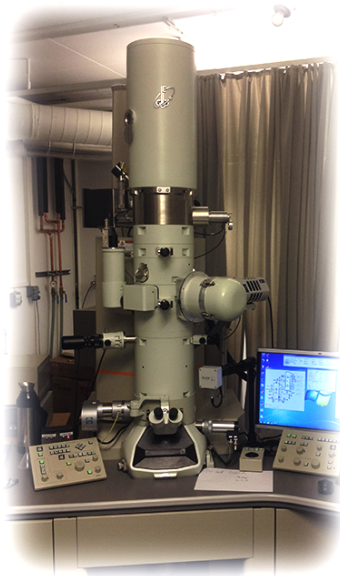
Figure 4.2: The Jeol 2100F in Forskningsparken.

(1 pm = 10^{-12} meter), neglecting relativistic effects. The spatial resolution of a TEM is therefore not limited by the electron wavelength. It is however limited by the quality of the electromagnetic lenses [47, p. 6]. The Jeol 2100F used in this project work has a spatial resolution of 1.9 Å [48].

4.2.2 The instrument

The TEM consists of an electron source, electromagnetic lenses, a sample holder, a viewing screen, and various detectors. The different parts are stacked vertically in a column which is maintained at high vacuum. Figure 4.2 shows the Jeol 2100F used in this thesis.

The electron source is situated on top of the column, and in most modern TEMs this is a field emission gun. In a field emission gun, electrons tunnel out from the tip of the gun due to a high voltage provided by an anode. A second anode accelerates the electrons to the desired energy, typically 200 keV. The electrons are converged, focused, and magnified by electromagnetic lenses in the column. The condenser lenses are located below the electron source, and act to converge the electrons to a desired spot size onto the sample. The electrons then interact with, and transmit through the sample. The objective lens (Figure 4.3) produces an image of the sample, which is magnified by intermediate lenses, and projected onto a fluorescent screen by a projector lens. The fluorescent screen absorbs the electrons, and produces visible light which can be viewed by the human eye. Digital images can be acquired by an electron-sensitive CCD camera which is inserted into the column in one of the intermediate image planes. The CCD camera utilised in this thesis, is an Orius SC 1000W.
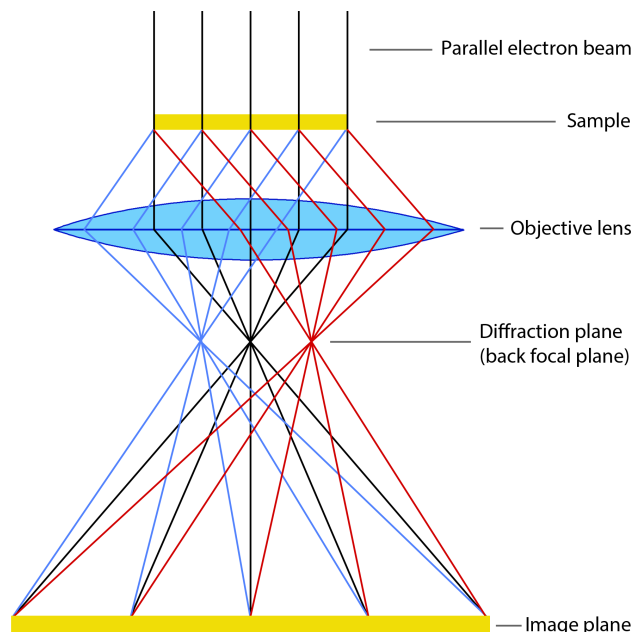
Figure 4.3: The objective lens converges all electrons from one point on the sample to one point in the image plane. It also converges all electron spread to a specific angle into a point in its back focal plane.

4.2.3   Image mode

As electrons from the gun transmit through the sample, they may interact with the sample's electrons and atomic nuclei. This results in various signals, represented in Figure 4.4. These signals can be used by different detectors to learn about the sample. The interactions cause the incoming electrons to deviate from their original path, lose energy, or they can be absorbed, and this gives contrast to the image of the sample. The objective lens converges all electrons from one point at the sample to one point in its image plane. This image can be projected onto the fluorescent viewing screen or the CCD camera, where one sees a 2D projected image of the sample with contrast resulting from the different interactions. This is referred to as *image mode*.

4.2.4   Diffraction mode

The incoming electrons are spread by the sample via elastic and inelastic scattering processes, which in general are referred to as electron diffraction. Only elastically scattered electrons will be considered in this section, as inelastically scattered electrons generally act to produce noise in images and diffraction patterns [49, p. 10]. Inelastically scattered electrons are however crucial for electron energy loss spectroscopy, which is the topic of the next section. The elastically scattered electrons are scattered in all directions, but since electrons have wave properties, they may interfere constructively for certain scattering angles. This constructive interference is referred to as *Bragg diffraction* [47, p. 49], and arises from atomic planes in crystalline materials, see Figure 4.5. Constructive interference happens when the *Bragg*
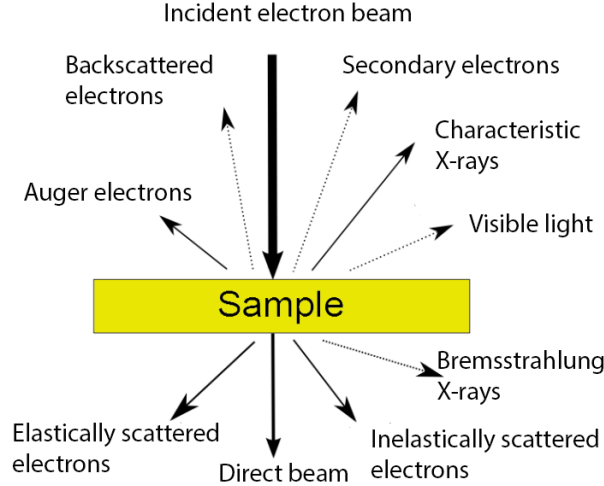
Figure 4.4: The different signals generated by interactions between incoming electrons and the sample.

condition is fulfilled, given by *Bragg's law*:

$$2dsin(\theta) = n\lambda \tag{4.3}$$

where d is the distance between the diffracting planes, θ is the diffraction angle for constructive interference (or *Bragg angle*), λ is the electron's wavelength, and n is an integer. When the Bragg condition is fulfilled, the path distance between two electrons scattered by parallel planes equals an integer number of electron wavelengths for a certain angle. Constructive interference thus occurs for that particular angle, the *Bragg angle*. All electrons that are spread by the sample into a given angle are converged to one point in the objective lens' back focal plane, or *diffraction plane*. By changing the current in the electromagnetic lenses, and thus their strengths, the resulting *diffraction pattern* can be projected onto the viewing screen or the CCD camera. An example of a diffraction pattern is found in Figure 5.2 b). The diffraction pattern is a Fourier transform of the sample image, and so it exists in *reciprocal space*, where the units are [length^{-1}].

Each spot (or *reflection*) in the diffraction pattern is the result of elastic scattering from a particular set of atomic planes that satisfy the Bragg condition. The diffraction patterns may be indexed to show what reflections result from what planes in the crystal. This has been done in Figure 5.2 c). The indexing procedure requires knowledge about the *camera length* of the microscope when the diffraction pattern was acquired, in addition to knowledge about the *structure factor* of the material one is working with. The structure factor is a mathematical description of what reflections are possible from a specific crystal system. Kittel's book on solid state physics [8] explains this in detail. Figure 4.6 shows the relation between the camera length, the distance between the diffraction spots, and the Bragg angle. The scattering angles are very small in a TEM, on the order of milliradians, so the assumption that $tan(\theta) \approx sin(\theta)$ can be made. Combining this assumption with the geometry in Figure 4.6 and Equation 4.3, one arrives at the following relation.
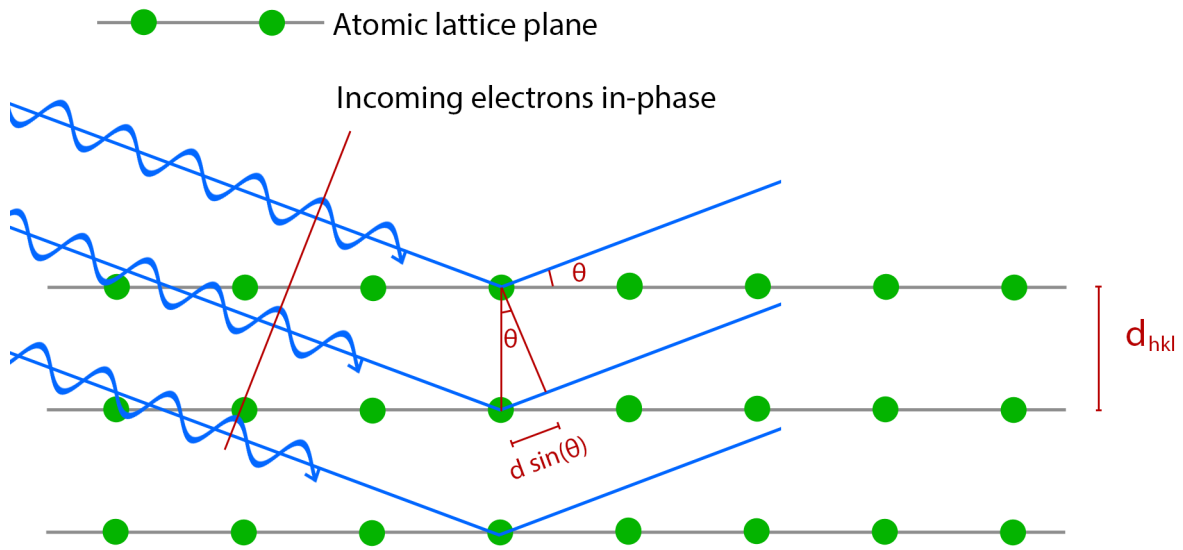
$$Rd = \lambda L \tag{4.4}$$

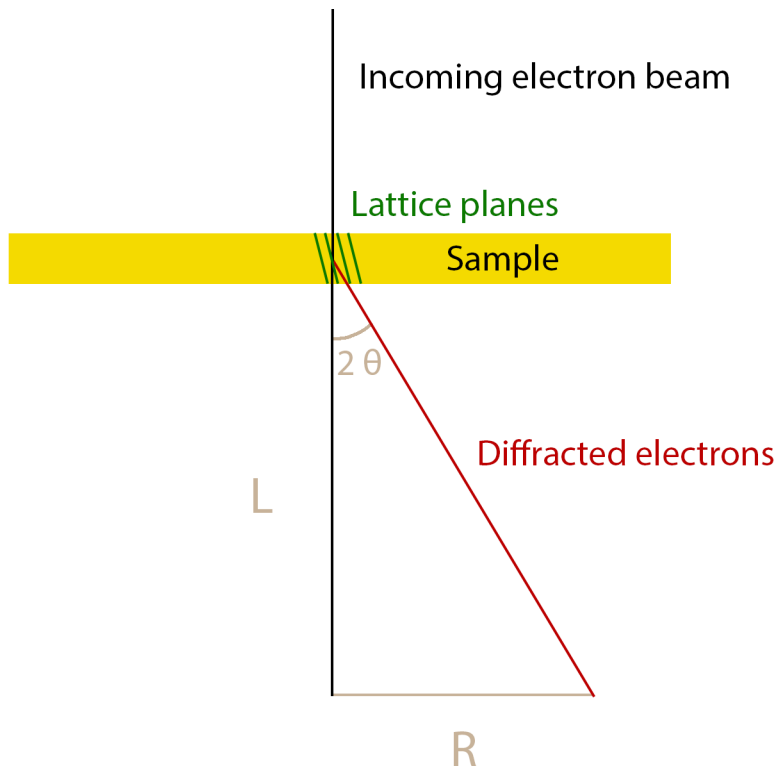Figure 4.5: The diffracted electrons will be in-phase if Bragg's law (Equation 4.3) is fulfilled.

Figure 4.6: Schematic illustration of the camera length L, the distance between the diffraction spots R, and the Bragg angle θ.

For cubic systems, one has

$$d_{hkl} = \frac{a}{\sqrt{h^2 + k^2 + l^2}} \tag{4.5}$$

where h, k, l are the Miller indexes of the plane, d_{hkl} is the planar distance between the hkl-plane, and a is the lattice parameter of the crystal [49, p. 15]. One can therefore deduce the lattice parameter of a material with known structure factor from the diffraction pattern. The diffraction patterns are presented in colour inverted form in this report, to reveal the weaker spots (reflections). When more reflections are revealed, one can get a more exact estimation of the reflection distances (d_{hkl}, or "spot distances"), and thus also the calculated lattice parameter. When measuring over several spots, the total length is divided by the number of gaps between spots that were included. This gives an average spot distance over which the measurement was done, and is more accurate than a single spot distance measurement. This will be done for pure as well as boron implanted 3C-SiC in this thesis.

The following experimental parameters have been used when obtaining diffraction patterns:

- Convergence aperture 1

- Selected area aperture 2

- Parallell electron beam

- Camera length 80 cm for all calculations

4.2.5 HRTEM

High resolution TEM (HRTEM) refers to operating conditions which allow for atomic scale detail in image mode, through extensive magnification and careful alignments. In addition to precise calibrations of the microscope, the sample must be tilted to a *zone axis* (ZA). A zone axis is a high-symmetry orientation in the crystal, such that a row of atoms are projected as one point along the ZA vector. This is illustrated for the [101] ZA in 3C-SiC in Figure 4.7.
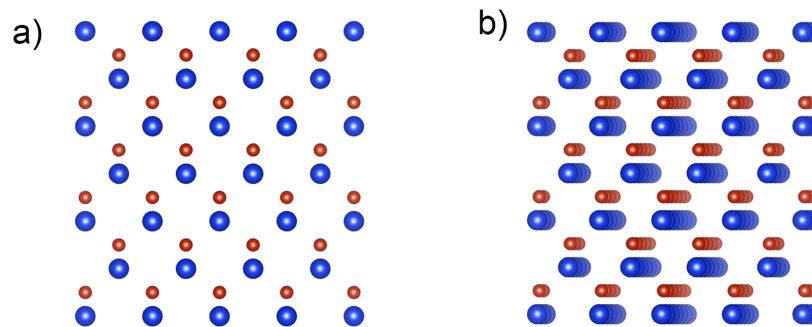

Figure 4.7: Good alignment with a zone axis is crucial for HRTEM. The illustration shows how the atoms in the 3C-SiC crystal line up when tilted to the [101] ZA. a) shows perfect alignment, and b) shows an off-axis situation.

When the sample is tilted to a ZA one can see individual rows of atoms as dots in the image, as in Figure 5.2. What actually is seen in HRTEM images is the phase contrast from interference of electrons, scattered by the atomic lattice. It is not straight forward to deduce wether the white dots actually correspond to single or multiple atomic rows, or the voids between them. This can be calculated using the *multislice method* [47, p. 533], knowing the settings of the microscope and the thickness of the sample. Defects on the atomic scale may in any case be seen at atomic resolution by HRTEM, and so it is a valuable technique which is used in this thesis. The [101] ZA has been used for HRTEM in this work. That specific ZA was chosen because the lattice projection along this direction in the zincblende system gives the biggest interatomic spacings. Still, the 1.9 Å resolution in the Jeol 2100F is insufficient to resolve the Si and C atoms as distinct, so they appear as one point in all atomic resolution images in this thesis.

4.3 Electron energy loss spectroscopy

Electron energy loss spectroscopy (EELS) is an experimental method for measuring the inelastic energy losses experienced by TEM electrons after interaction with the sample. The EELS detector is placed at the bottom of the TEM column. Most electrons pass through the sample without losing energy, but as illustrated in Figure 4.8, several characteristic peaks of electron energy loss occur for a given material.
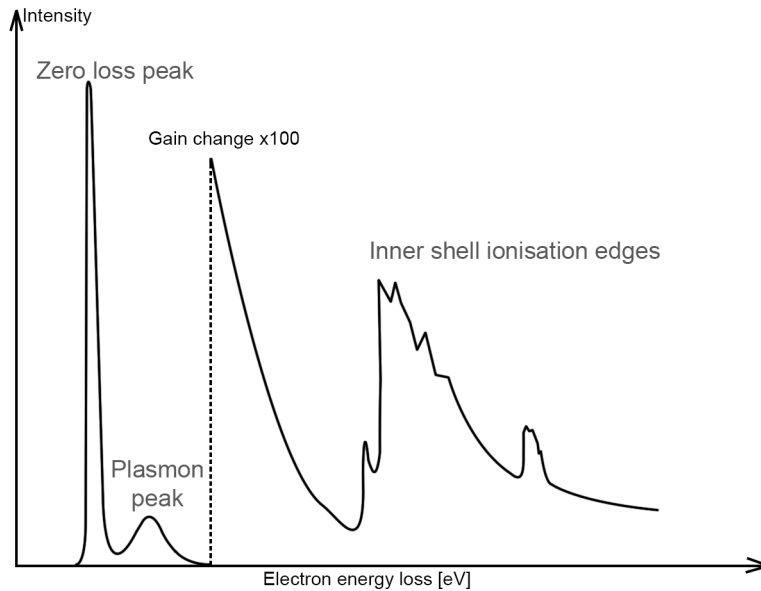
Figure 4.8: A generic electron energy loss spectrum. Figure adapted from [50].

The zero loss peak (ZLP) contains the electrons that have not experienced an energy loss, that is all non-scattered, and elastically scattered electrons. The second most intense peak in EELS is the plasmon peak for most materials. Plasmons are collective oscillations of electrons in the outermost orbitals, and these oscillations can absorb energy from incoming, high energy electrons. The plasmon peak (E_p), as measured in energy loss [eV], can be

estimated through

$$E_p = \hbar \left(\frac{ne^2}{\epsilon_0 m_e} \right)^{\frac{1}{2}} \tag{4.6}$$

where $\hbar$ is the reduced Planck constant, n is the valence electron density, e the elementary charge (-1.6022·10^{-19} C), e_0 the permittivity of free space (8.8542·10^{-12} F/m), and m_e the electron mass (9.1094·10^{-31} kg) [47, p. 707]. This equation assumes free electrons, i.e. not bound to any specific ion or atom. Note that the only non-constant value in Equation 4.6 is the valence electron density. The width of the plasmon peak depends on the rate of decay of oscillations [50]. The ZLP and the plasmon peak are both located in what is referred to as the *low loss* part of the spectrum, which usually is defined to be 0 - 50 eV energy loss. The *high loss* part of the spectrum (50 eV $\rightarrow$), has an exponentially decaying background signal, plus the inner shell ionisation edges.

The inner shell ionisation edges are, as the name implies, caused by excitations of core electrons in the sample into available electron states above the Fermi level. The details of the ionisation edges are referred to as electron energy loss near-edge structure (ELNES). Since the energy levels of core electrons are characteristic for a given element, one can directly identify elements in the sample from the observed inner shell ionisation edges. The ELNES also contains information about interatomic bonding, and the density of electron states (DOS). This is because core electrons are localised in energy, and may be excited into any available state above the Fermi level. Changes in a material's DOS, and thus the ELENS spectra, will occur with changes in chemistry and structure. It is therefore expected that boron implantation will alter the silicon and carbon ionisation edges.

The EEL spectrometer used in this project is the Gatan GIF 963. When operating the detector, one selects the desired energy range to get either low loss, or core loss spectra. For Si, the L_2 (99.80 eV energy loss) and L_3 (99.20 eV energy loss) ionisation edges overlap, and the combined edge is referred to as Si $L_{2,3}$. The carbon K edge is at 284 eV energy loss, and the boron K edge at 188 eV energy loss.

There are many experimental parameters that affect the shape and intensity of EEL spectra. Consistency in experimental conditions is therefore crucial. The following parameters have been used when obtaining EEL spectra.

- Sample thickness of 0.2 - 0.4 mean free paths for inelastic scattering

- Spot size 5, converged to cover the inner square of the fluorescent screen at 500 kX

- Diffraction mode with camera length of 60 cm

- Convergence aperture 1

- Energy dispersion of 0.1 eV/channel on the CCD

- Collection aperture of 2.5 cm

- Exposure times of 0.01 - 0.05 s for low loss, and 2 - 8 s for high loss spectra
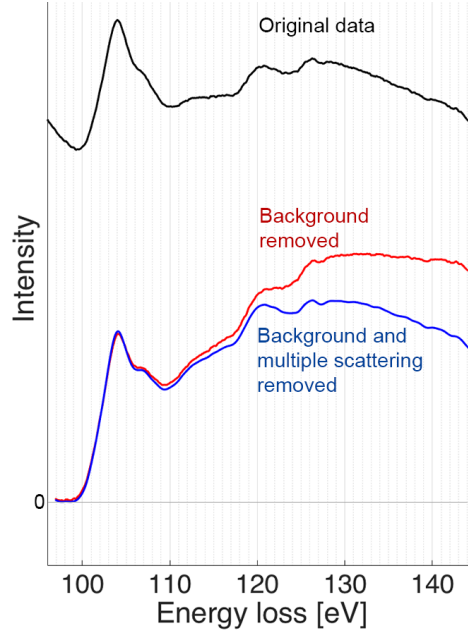
Figure 4.9: The effects of background removal and multiple scattering removal on the Si $L_{2,3}$ edge in 3C-SiC.

All spectra consist of multiple exposure added together for better counting statistics; typically 100 exposures for low loss, and 30 exposures for high loss spectra. The energy resolution has been 1.0 - 1.2 eV, measured as the full width at half maximum of the ZLP.

4.3.1 Experimental EELS data processing

In order to extract the real ELNES signal from an experimental EEL spectrum, the background signal must first be removed. This was done in the TEM analysis software Digital Micrograph. The software fits a pure *power law background model* in a user-selected energy window before edge onset, extrapolates it over the whole spectrum, and removes it. Multiple electron scattering also deteriorates the true ELNES signal. If for instance a TEM electron first loses energy to a plasmon excitation, and secondly to a core ionisation, the resulting spectrum will be distorted. This problem becomes more significant with increasing sample thickness. Multiple scattering effects are digitally removed using Digital Micrograph with the *Fourier-ratio algorithm* in the EELS package. The Fourier-ratio algorithm uses a low-loss spectrum obtained at the same sample area with the same experimental conditions as the core loss spectrum, to remove the multiple scattering effects from the latter. The effects of background, and multiple scattering removal are illustrated in Figure 4.9. Both these procedures are necessary for comparison of experimental ELNES to simulated spectra, since the latter only contains the true ELNES signal. The downside to performing these alterations to the experimental data is that one might introduce artefacts to the spectrum. Care must therefore be taken to always use the same processing procedure for all spectra when removing background and multiple scattering effects.

4.4 ELNES simulations using Feff

Feff is an automated Green's Function code for *ab initio* multiple scattering calculations of ELNES spectra, and related quantities [6]. ELNES simulations have the potential to reveal changes in chemistry and structure when analysed together with experimental core loss spectra. If there is an experimental change between for example pure and implanted 3C-SiC, one can controllably simulate alterations to structure and/or chemistry in Feff, and look for similar changes in simulated spectra.

Feff performs a number of calculations to output electron loss spectra based on a cluster of atoms, provided by an input file. The input file is made by the user, and includes commands, parameters and a list of the desired structure's atoms and their respective coordinates. An example of such an input file is found in the appendix, Figure B.4. Several parameters need to be converged for realistic ELNES simulations. The process for achieving this is presented in Subsection 5.7.1.

The following roughly describes Feff's data flow with emphasis on a few important points. The code starts by calculating atomic potentials for a desired cluster size, using self consistent field (SCF) iterations. When convergence is reached, one has the Fermi level of the cluster. The local density of states (*ldos*) for each unique potential in the cluster (Si, C and B in the case of this thesis) is then calculated. A *full multiple scattering* (FMS) algorithm is performed on a desired cluster size, to calculate all possible paths the excited electron might follow. Its final state is a superposition of all of these. A number of intermediate calculations is then done, before the ELNES simulation concludes the work and produces an output electron energy loss spectrum. A more comprehensive data flow description is given in Feff's user manual, reference [51].

4.4.1 Simulated EELS data processing

The silicon L_2 and L_3 edges are simulated individually in Feff. Their energy onsets are very similar; 99.80 eV energy loss for L_2, and 99.20 eV energy loss for L_2, which means that the two edges overlap in experimental spectra. The interpolating function *interp1* in Matlab was used to combine the simulated L_2 and L_3 edges into an $L_{2,3}$ edge (script found in in Figure B.2 in the appendix). This is not a concern with the carbon K edge, which does not overlap with other silicon, carbon or boron ionisation energies.

While Feff produces simulated spectra with precisely defined energy losses, the experimental spectra are more smeared out. This is due to, and determined by the shape of the zero loss peak, which can be assumed to have a gaussian-like character. In an ideal monochromated TEM, the zero loss peak (ZLP) would contain electrons of only one precise energy, but this is not the case for real microscopes. The full width half maximum (FWHM) of the ZLP has in all experiments been between 1.0 and 1.2 eV. The simulated spectra have therefore been convoluted with a gaussian function to replicate this experimental smearing. Matlab's *gaussmf* was used for the gaussian function, and the *conv* function was used for the convolution (script found in in Figure B.2). The ZLP is in fact not totally gaussian, but
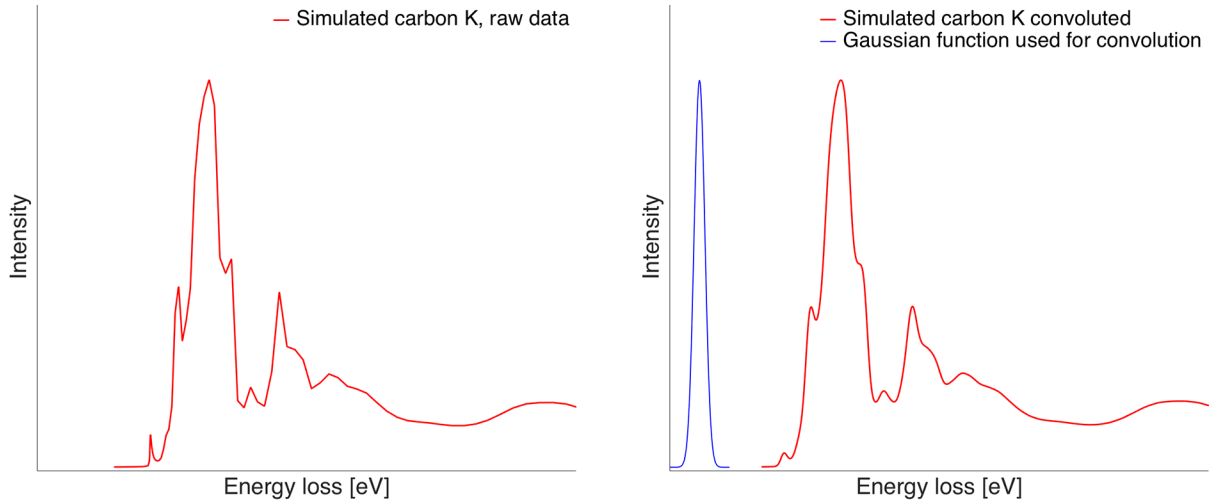
Figure 4.10: The effect of a gaussian convolution on the Si L_2 edge in 3C-SiC

this is a good approximation, and the result is seen in Figure 4.10 for the carbon K edge in 3C-SiC. The gaussian function's standard deviation was chosen based on the best fit with experimental results.

The standard procedure when normalising EEL spectra is to normalise with respect to the background intensity tail. This is however not possible for simulated spectra, as they are ideal with no background intensity. A simple normalising has therefore been performed so that the maximum intensity is unity in all experimental and simulated spectra.

4.5 Boron implantation and annealing

Ion implantation was performed on SiC samples by UiO senior engineer Viktor Bobal at MiNalab. Implantation temperature was 400°C, and eight different implantation energies were chosen to reach different depths below the surface. These were 100 keV for 200 nm, 160 keV for 300nm, 225 keV for 400 nm, 300 keV for 500 nm, 375 keV for 600 nm, 475 keV for 700 nm, and 575 keV for 800 nm below the surface. This has been confirmed to give an even concentration of boron in the top 200-800 nm, using secondary ion mass spectroscopy (SIMS). All SIMS measurements were performed by UiO scientist Quanbao Ma. He has also been responsible for annealing, which was done at MiNalab using a crucible at 1400°C for one hour.

Chapter 5

Results and Discussion

This chapter presents the data obtained, and the work done to fulfil the objectives stated in the introduction. The results are discussed consecutively.

5.1 Samples

As explained in Section 3.2.2, a varying amount of domain phase boundaries occur in all samples grown by the Linköping group. Investigation of DPBs is not a concern of this thesis, and care was taken to prepare TEM samples from single domains in the crystals. In Figure 5.1 one can see domain phase boundaries stretching horizontally across a typical as-grown 3C-SiC crystal.

Several TEM samples were made during the thesis work, but only five were chosen to provide data for this chapter. Two of the five are focused ion beam-samples (FIB samples), and were prepared by SINTEF scientist Patricia Carvalho. An overview of the five samples is found in Table 5.1.

Table 5.1: Sample overview

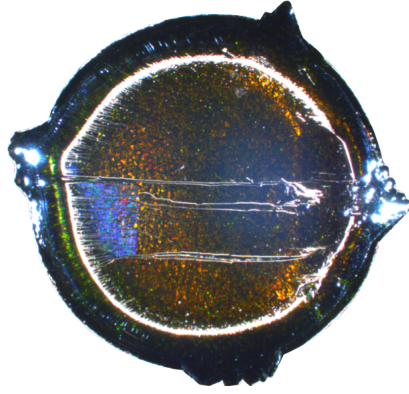| Name	Sample type	Polytype	Boron implantation	Annealing
1-1	Cross section	3C	No	No
2-1	FIB cross section	3C	Yes	No
3-1	Cross section	3C, 4H, 6H	Yes	1h at 1400°C
3-2	Cross section	3C	Yes	1h at 1400°C
3-3	FIB cross section	3C	Yes	1h at 1400°C

Figure 5.1: Optical microscopy image of domain phase boundaries in a typical 3C-SiC crystal grown at LiU.

5.2   Unimplanted 3C-SiC

Unimplanted, as-grown 3C-SiC was found to be largely defect free. Figure 5.2 is a representative HRTEM image from sample 1-1, and it shows perfect alignments of atoms along the 101 zone axis. Only two crystallographic defects, in the form of stacking faults, were found in sample 1-1. A stacking fault is a local deviation in the stacking sequence of atomic layers in a crystal. The stacking faults were found to span several micrometers. One of the two is imaged at atomic resolution in Figure 5.3. The bent shapes in 5.3 c) are bending contours, and are caused by curvature of the sample due to ion milling. Bending contours are easy to distinguish from stacking faults because they change in appearance when moving the sample, while stacking faults are static during TEM investigation. As the stacking faults were detectable at low magnifications, they were easily countable. The stacking fault energy in 3C-SiC has been found to be negative [54, 55] so their presence is not a surprise; the surprise is rather their apparent rarity. The near absence of crystallographic defects in sample 1-1 confirms the assertion by the Linköping group [5] in that they have achieved domains of high quality single-crystalline 3C-SiC.
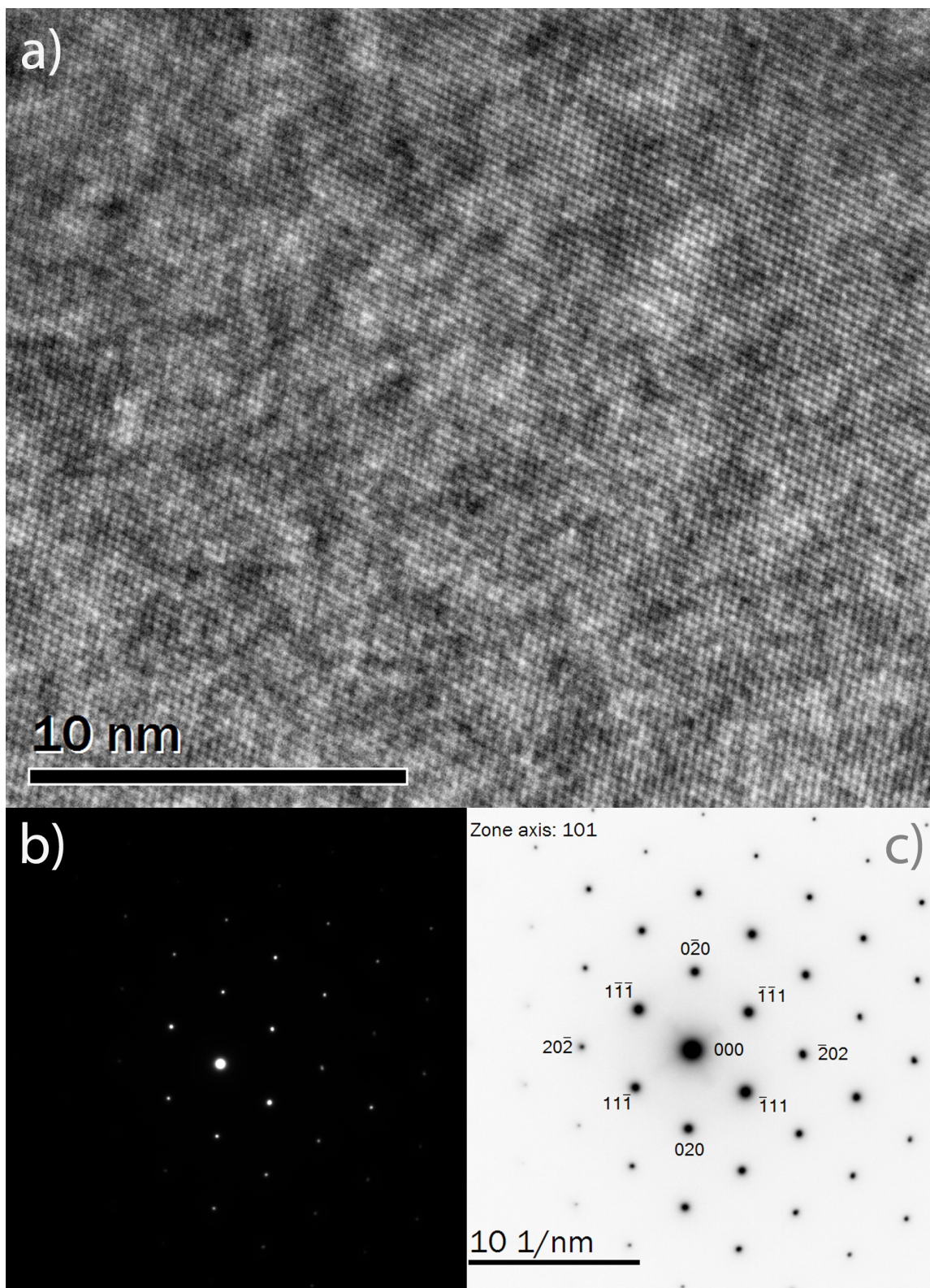
Figure 5.2: a) A representative defect free atomic resolution image of unimplanted 3C-SiC. Grey tone variations is due to an amorphous sample surface, resulting from ion milling. The corresponding inserted diffraction pattern in b), is colour inverted and indexed in c).
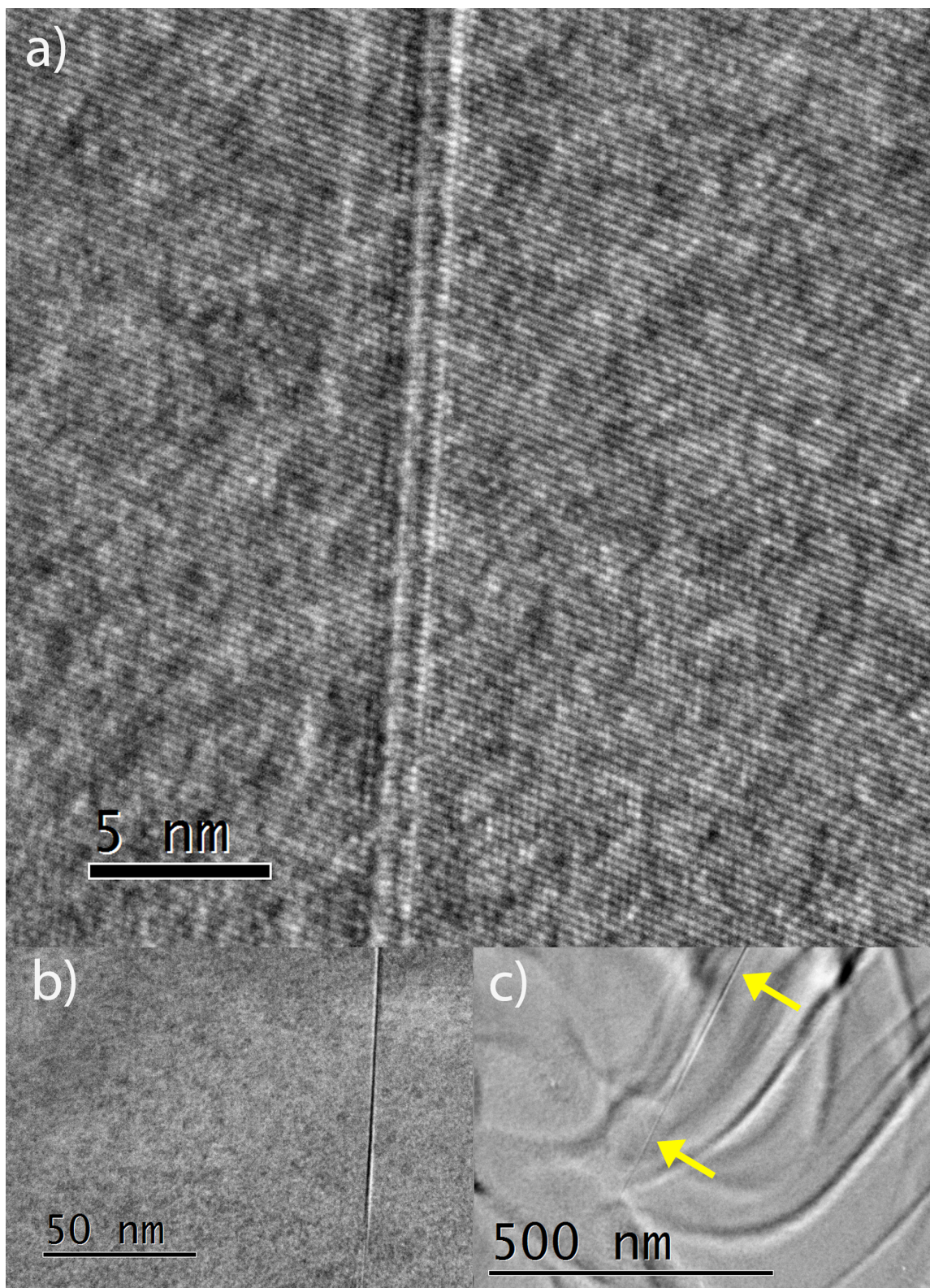
Figure 5.3: One of two stacking faults found in sample 1-1. a) Shows the stacking fault resolved at atomic resolution. In b) it is still clearly visible at lower magnification, and in c) it is also apparent, indicated by arrows, among bending contours. Bending contours result from sample shape, and are not defect-related.

5.3 Boron implanted 3C-SiC

Boron implantation is the essential factor for achieving the hypothesised intermediate band. Sample 2-1 was made using FIB from 2 at% boron implanted 3C-SiC. Figure 5.4 is an overview image of the implanted layer. The boron implantation has clearly amorphised the 3C-SiC, as seen from the inserted diffraction pattern. Diffuse, concentric rings in the diffraction pattern is the hallmark of an amorphous structure. The crystal structure beneath the implanted layer remains undamaged, and the transition between crystalline and amorphous SiC is abrupt. The amorphisation of the implanted layer is in the case of *SunSiC* unwanted as the 3C crystal structure is not maintained. Amorphisation is however a common problem with ion implantation at large doses [56]. Carl McHarguc and J.M. Williams found when implanting Cr and N into 6H-SiC, that increasing implantation temperatures from room temperature up to 750°C, the degree of amorphisation resulting from implantation was significantly reduced [57]. Ion implantation has in this project been performed at 400°C, and increasing the temperature might help to combat the amorphisation.
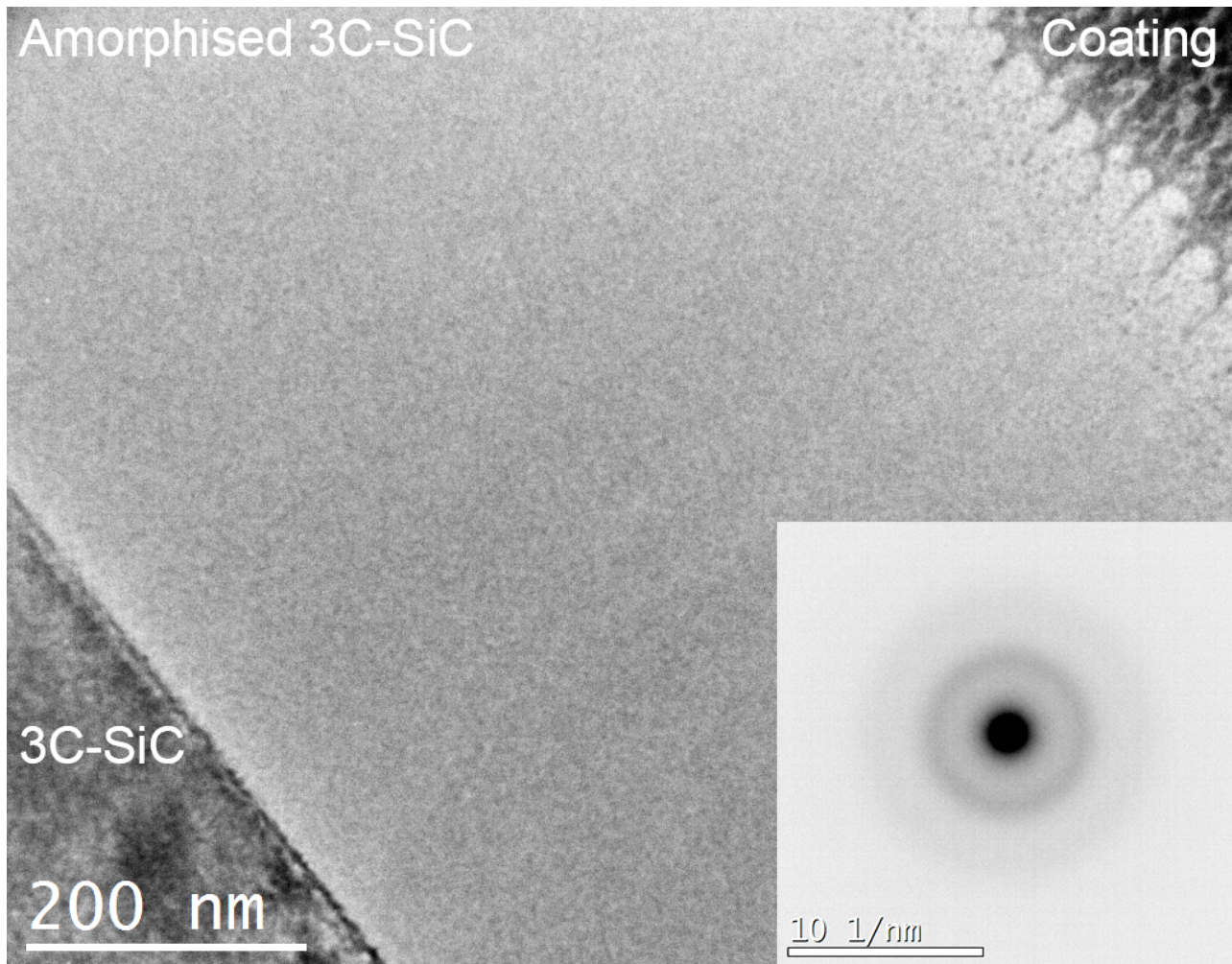

Figure 5.4: Overview image of sample 2-1 with inserted diffraction pattern, obtained from the middle of the amorphous region.

5.4 Annealed, boron implanted 3C-SiC & hypotheses

Heat treatment (annealing) is a common technique for recrystallising amorphised crystals. Recall that the goal of this thesis is to understand how boron implantation and subsequent annealing affects the atomic structure of 3C-SiC. The following hypotheses on how the boron possibly might distribute in 3C-SiC after annealing can be formulated at this stage. They will later be referred to as hypotheses 1 through 4.

1. Boron might substitute carbon or silicon, or both.

2. Boron might take interstitial positions in the lattice.

3. Boron might cluster and form pure boron precipitates.

4. Boron might form phases with Si or C, or both.

TEM and HRTEM images of implanted and annealed samples are presented and discussed firstly. Supplementary TEM techniques for further testing the hypotheses are presented thereafter.

5.5 TEM and HRTEM images

TEM investigation of annealed, 3 at% boron implanted samples (sample 3-1, 3-2 and 3-3) reveals complete recrystallisation of the implanted layer after 1 hour at 1400°C. Figure 5.5 gives an overview of the recrystallised layer in sample 3-3, tilted to the 101 zone axis. Defects are easily detectable at this orientation even at low magnifications, as is apparent from the figure. The top region of approximately 100 nm to the upper right in Figure 5.5 is defect free like the as-grown 3C-SiC crystal, and this was found to be the case for all implanted and annealed samples. This was somewhat of a surprise. One might think that the top layer would be the most damaged from implantation, since all implanted ions penetrate the top layer before coming to rest deeper in the material. This is clearly not the case, and the defects cannot be due to implantation damage. A secondary ion mass spectroscopy (SIMS) depth profile corresponding to sample 3-3, Figure 5.6, shows that the boron concentration reaches 10^{21} atoms/cm^3 (corresponding to 3 at% boron) at 200-900 nm depth. As the boron concentration is significantly lower (10^{19} - 10^{20} atoms/cm^3) in the defect free sample surface, it can be assumed that the defects in the middle region of Figure 5.5 are related to the high boron concentration. Implications of this will be discussed later.

When planar defects are oriented parallel to the electron beam, they cause streaks in the diffraction pattern [47, p. 277]. Such streaks are present in the inserted diffraction pattern from the implanted region in Figure 5.5, and this suggest that the defects seen in the figure are planar. These planar defects were investigated further at atomic resolution in sample 3-2. Figure 5.7 shows that the planar defects causing streaks in the diffraction pattern are stacking faults. The stacking faults are typically 20-80 nm in length, as opposed to the as-grown stacking faults which have lengths on the order of micrometers. The stacking fault in Figure 5.7 b) is an extrinsic stacking fault, i.e. an addition of a close-packed layer in the
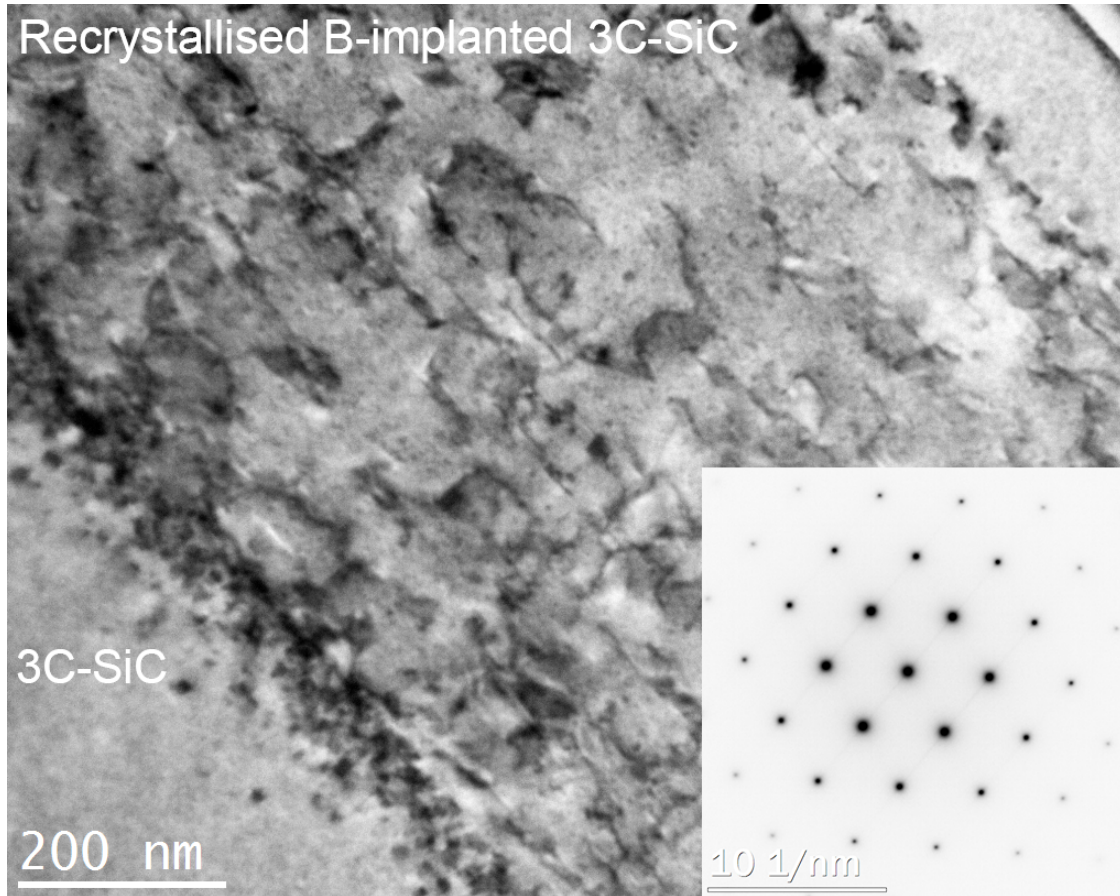
Figure 5.5: Overview image of sample 3-2 displaying a high defect concentration relative to unimplanted samples. Notice the defect-free top 100 nm to the upper right, and the streaks in the diffraction pattern. The image is representative for all implanted, annealed samples.
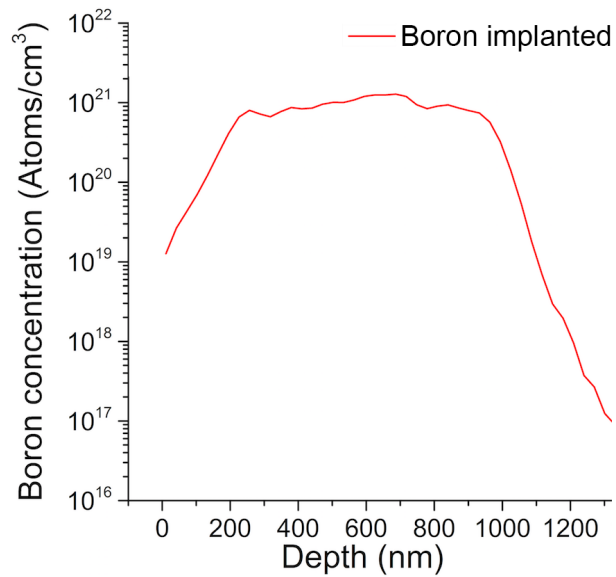
Figure 5.6: Secondary ion mass spectroscopy depth profile of sample 3-2.
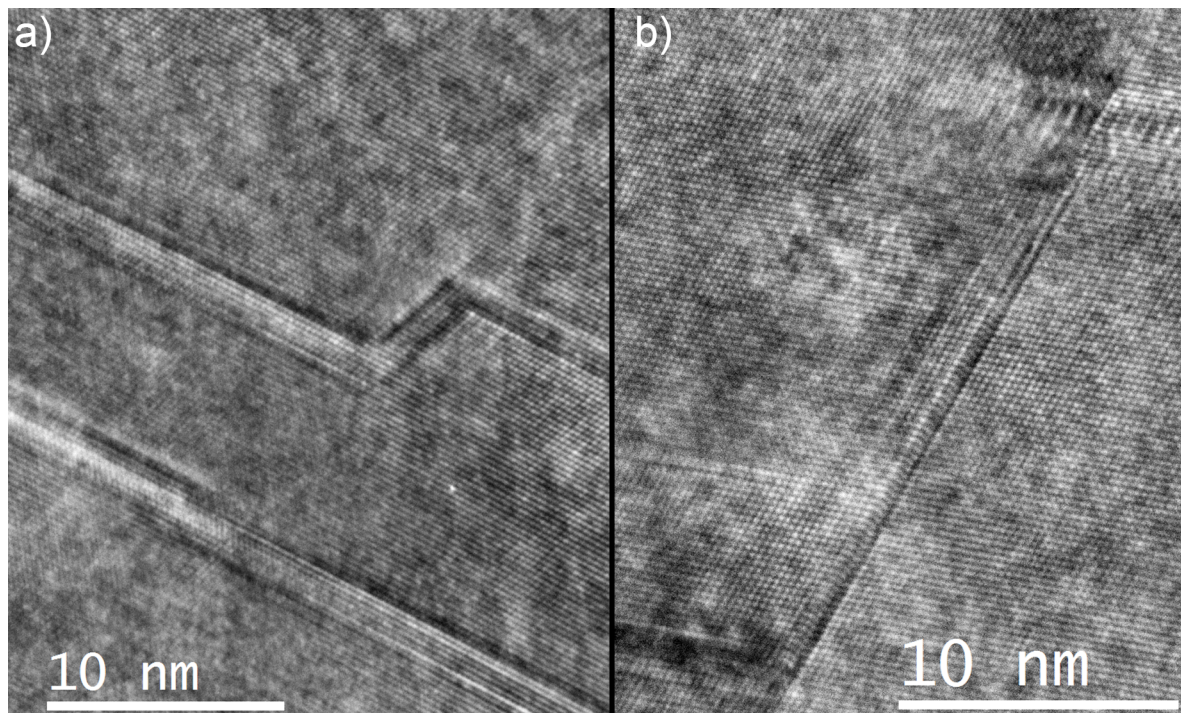
Figure 5.7: Atomic resolution images show that the defects visible in Figure 5.5 are stacking faults.
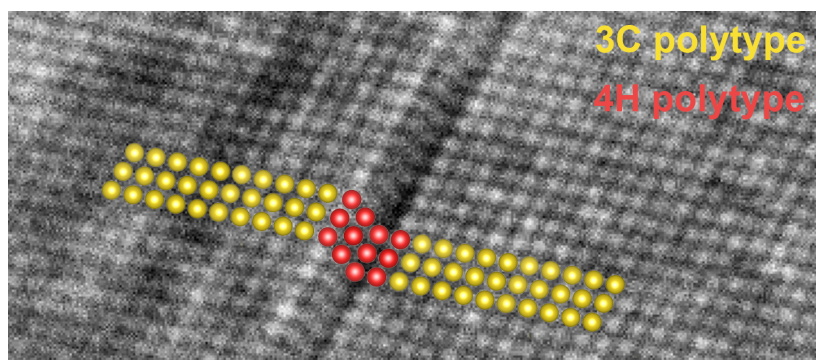
Figure 5.8: An extrinsic stacking fault from Figure 5.7 b) viewed as a local layer of 4H-SiC. The overlaid dots are .cif files from the Pearson's Crystal Database [58] of the 3C and 4H polytype, tilted to the cubic [101] ZA and hexagonal $<1\bar{1}20>$ ZA in VESTA. Each dot represents a silicon and a carbon atom together, since the spatial resolution in the Jeol 2100F is insufficient to resolve these as individual.

stacking sequence (ACB to ACAB). This can be regarded as a local single layer of 4H-SiC, visualised in Figure 5.8. Stacking faults are known to alter the local electron band structure in semiconductors [59]. This is likely also the case for the stacking fault (4H monolayer) in Figure 5.8, considering that the band structures of 3C and 4H-SiC are quite unlike each other (Figure B.1). Depending on the interactions between the 3C/4H interfaces, the stacking fault might act as a quantum well, or an energy barrier. The exact character of the alterations to the band structure is difficult to predict without thorough density functional theory (DFT) calculations. It is however likely that the alterations will be unwanted in a solar cell material, since quantum wells generally act to increase carrier recombinations, and energy barriers lower the electron and hole mobilities.

The implanted regions (upper 200 - 900 nm) of samples 3-1, 3-2 and 3-3 were found to be single crystalline despite what one might suspect from Figure 5.5. No grain boundaries were found, and the crystal orientation in the implanted and unimplanted regions were found to be the same, using diffraction. This is a peculiar finding, since the pre-annealed implanted region in sample 2-1 appears completely amorphous. If this was the case, one would expect grains of random crystal orientation after annealing. An explanation for the post-annealed single crystallinity could be that the unimplanted 3C-SiC (900 nm and below) acts as a seed crystal during recrystallisation. Also, the short range order might be intact after implantation, while the long range order is not maintained. This could give the diffraction pattern an amorphous character, as is observed, while the pre-implanted crystal orientation would be preferential during recrystallisation. The single crystallinity is in any case desired for solar cell applications, independent of the explanation.

Atomic resolution images from the implanted recrystallised layer also reveal moiré fringes in circular and oval features. Moiré fringes in HRTEM is a visual interference effect resulting from two lattices that are rotated and/or translated with respect to each other. The presence of moiré fringes, as seen in Figure 5.9, shows that there are precipitates in the recrystallised region. These precipitates were found to be oval shaped, and 10-30 nm in diameter. This makes them too small for selected area diffraction, and so phase identification could not be done from diffraction. Energy-dispersive X-ray spectroscopy (EDS) analysis was attempted, and only carbon and silicon was detected. This does not mean that boron is not present in the precipitate, since boron is at the very edge of EDS detectability due to its very low fluorescence yield. To identify the likely phase of the precipitate, it was found useful to consider the ternary phase diagram for silicon, carbon and boron. The phase diagram found in the appendix, Figure B.5, is for 1414°C; quite close to the annealing temperature of 1400°C. From the diagram, one can see that SiC with 3 at% boron (indicated by a red cross) is very close to the SiC/$B_{13}C_2$ two-phase region. This indicates that the two phases coexist in equilibrium at the given temperature, and that the likely phase of the observed precipitates is $B_{13}C_2$. This conclusion is further supported by published papers on boron doped 4H- and 6H-SiC [64, 65]. Similar precipitates were found in [64, 65], and it was concluded that $B_{13}C_2$ is the most likely phase, although $Si_{10}B_{60}$ was not excluded as a possibility. Nevertheless, it seems reasonable that hypothesis 3 (pure boron precipitates) can be discarded in favour of hypothesis 4 (precipitate boron phases with silicon and/or carbon).
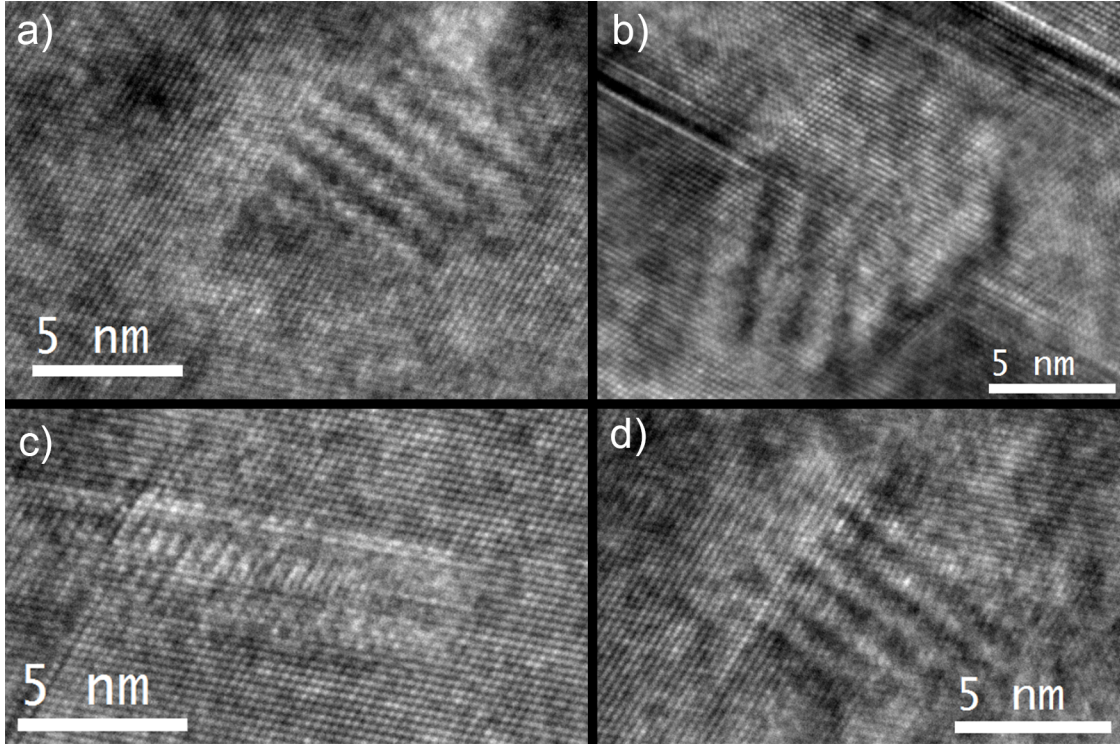
Figure 5.9: Moiré fringes in HRTEM images from sample 3-2. In c) there are no fringes, probably because the precipitate extends through the sample thickness.

The intermediate band in 3C-SiC has been theorised to arise from boron atoms forming delocalised deep energy levels, not from precipitates of new phases. Annealing, and thus formation of precipitates, must however be performed to regain crystallinity of the implanted layer. The solid solubility of boron in 4H-SiC has been found to be $1*10^{20}$ cm^{-3} [65]. This corresponds to approximately one thousandth of the concentration determined by SIMS for sample 3-3. If boron solid solubility in 3C-SiC and 4H-SiC are similar, it would mean that the current implantation dose goes well beyond saturation. The formation of boron-rich precipitate phases is therefore expected, since the lattice is supersaturated. Diffusion increases at elevated temperatures, and boron-rich phases can therefore easily form during annealing. A significant lowering of the boron implantation dose will probably still result in the maximum solid solubility of boron, but fewer precipitates.

The atomic (covalent) radii of boron, carbon and silicon are 84 pm, 76 pm and 111 pm, respectively [60]. One nanometer (nm) equals 1000 picometers (pm). Hypothesis 2 is on that basis unlikely, as the atomic radius of an interstitial impurity must be substantially smaller than that of the host atoms [61, p. 85]. While most of the implanted boron is probably found in the precipitates, there will likely also be some degree of substitutional boron in the lattice, in accordance with hypothesis 1. The following sections investigate the substitution hypothesis further.

5.6   Diffraction patterns

A change in a_{3C} with implantation is expected if the degree of substitutional boron in the 3C-SiC lattice is sufficient. Such a change can be measured by diffraction patterns and calculation with equations 4.4 and 4.5. If boron substitutes carbon in the lattice, there will according to Yo Tajima and W. Kingery [63] be a slight increase in the 6H-SiC lattice parameter. The effect was found to be opposite and larger if silicon is replaced. This is in accordance with what would be expected from a simplistic consideration of the atomic radii, and it should hold true also for 3C-SiC. However, DFT calculations performed by SINTEF scientist Ole Martin Løvvik show that the nature of the lattice parameter increase/decrease is dependent on the valence state of the implanted boron, in addition to the kind of atom replaced. The DFT calculations are for 3 at% boron, and the results are given in Table 5.2. It is assumed that the DFT calculations are more relevant for this discussion than the results of Yo Tajima and W. Kingery, because the former considers the correct polytype. It is also assumed that the substitutional boron takes valence state +1 in SiC, because boron is group III while silicon and carbon are group IV. On this basis, there should be a decrease in lattice parameter regardless of the kind of substitution, but the effect should be largest for substitution of silicon.

Table 5.2: DFT calculations of $a_{3C\text{-SiC}}$'s response to 3 at% boron substitution. Values are in picometers.

Substituted atom	Boron's valence state	$a_{3C\text{-SiC, implanted}}$	Relative change in $a_{3C\text{-SiC}}$
Pure 3C-SiC		437.81	
C	+ 1	437.04	- 0.77
C	0	438.92	+ 1.11
C	- 1	440.81	+ 3.00
Si	+ 1	434.51	- 3.30
Si	0	436.36	- 1.45
Si	- 1	438.23	+ 0.42

Table 5.3: The experimental lattice parameters from implanted and unimplanted samples. Values are in picometers.

Sample	# d_{hkl}-measurements	Mean a_{3C}	Std. deviation	Std. error in the mean
1-1	30	434.78	0.50	0.09
3-2	30	434.33	0.23	0.04

Diffraction patterns were obtained from samples 1-1 and 3-2 to detect the theorised change in lattice parameter with implantation. A camera length of 80 cm was used, which corresponds to a pixel resolution of 0.016 nm^{-1}, using the Orius CCD. This corresponds to 0.19 pm resolution in the calculated lattice parameter when measuring over four d_{hkl}-spacings, see Figure 5.10. Good counting statistics (many measurements) are required because the resolution (0.19 pm) is in the same order of magnitude as the theoretical changes in the lattice parameter. Assuming constant uncertainty in each measurement, one can get a precise
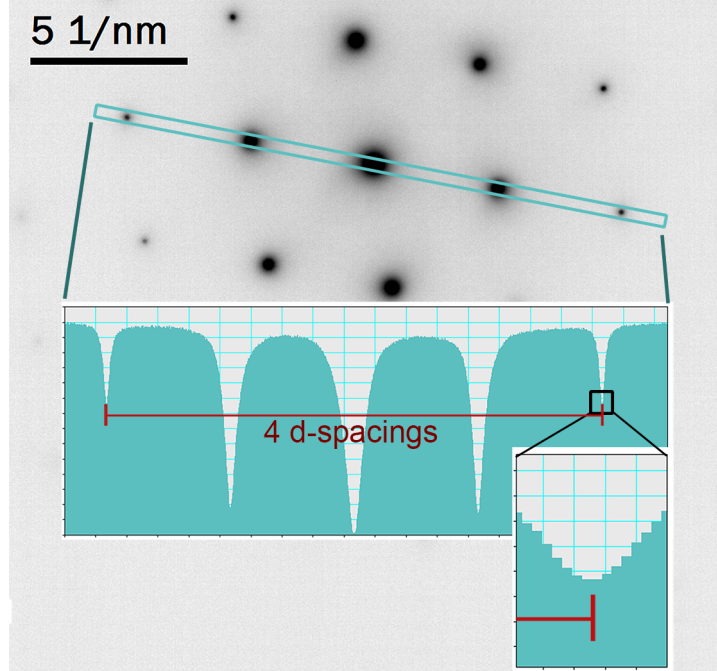
Figure 5.10: Four d_{hkl}-spacings were used in the experimental lattice parameter calculations. The pixel resolution is 0.016 nm^{-1}.

mean value with low *standard error in the mean* with many measurements. 30 individual d_{hkl}-measurements were done for both sample types, and the results are presented in Table 5.3. An experimental change in lattice parameter of negative 0.45 $\pm$ 0.13 pm was detected. DFT calculations (3 at% boron) predict a change of negative 0.77 pm for the replacement of carbon, and negative 3.30 pm for the replacement of silicon, but it has been argued that most of the boron is probably located in precipitates. This means that the changes predicted by DFT calculations are exaggerated with respect to the real situation in the implanted material. Boron substitution of silicon is thus most likely, considering the magnitude of the experimental shift resulting from the likely small amount of substitutional boron.

The experimental change in lattice parameter must however be considered with skepticism. The published literature value of a_{3C} ($a_{3C, \text{literature}}$) referred to in Chapter 3 is 435.91 $\pm$ 0.02 pm [39]; a deviation of 1.13 $\pm$ 0.11 pm from the experimental value in this thesis ($a_{3C, \text{experimental}}$). The cited reference used X-ray diffraction, and is in agreement with other publications. The deviation between $a_{3C, \text{literature}}$ and $a_{3C, \text{experimental}}$ is larger than the errors in the respective experiments account for. A systematic measurement error by the author is therefore likely. A systematic measurement error which is unchanged between different sets of data can lead to reliable results when looking at relative changes. It is however not possible in this case to know whether the (likely) systematic measurement error remained constant between the two sets of data. The same microscope settings (parallel beam, same apertures) were used for both samples. However, it is possible that slight alignment differences of the electron beam between the sessions has lead to different effective camera lengths, and thus skewed values.

5.7 Simulating ELNES using Feff

The nature of the boron distribution is further investigated by use of simulated and experimental EEL spectra. A basic Feff input file was generated at Web Atoms [52]. This web service generates atom lists of perfect structures. This means that one must manually edit the list (or write a script) to simulate implantations, defects, precipitates etc. Using Feff to achieve realistic ELNES simulations for a given material is not straight forward, and the procedure used by the author will be described before the actual output spectra.

5.7.1 Building the input file and converging parameters

The Feff input file generated at Web Atoms includes commands and parameters in addition to the real space cartesian list of atoms for the simulation. The parameters need to be converged for realistic simulations, and the two most important parameters are the self consistent field (SCF) parameter and the full multiple scattering (FMS) parameter. These have been explained in Section 4.4. The Web Atoms default value of 4 Å means that the FMS and SCF calculations only consider atoms within a sphere of radius 4 Å around the ionisation event when performing calculations. This is less than the unit cell parameter, a_{3C}. One cannot expect such a simulation to reflect reality, and so these parameters were increased at the cost of computing time. When increasing FMS and SCF to the range of 8-10 Å, it takes a personal computer more than 24 hours to complete the calculations. Convergence testing was a tedious process initially, but access to the Abel supercluster at UiO was granted in November 2015, and this made the process easier.

When increasing SCF stepwise from 5 Å to 11 Å, the Fermi level (found in the *ldos* output files) did not approach a stable value. One might expect convergence of the Fermi level when taking more and more atoms into account, but this did not happen conclusively for 3C-SiC simulations, although the change from SCF 10 to 11 is very small. SCF 11 is the maximum allowed value, so it was not possible to conclude that a decent convergence was reached at this value. A plot of the Fermi level with this stepwise SCF increase is given in Figure 5.11. There were also problems in converging the FMS parameter. Increasing FMS stepwise from 5 Å to the maximum allowed value of 13 Å did not provide a converging tendency in the density of states (in the *ldos* output file), nor the resulting ELNES spectra. A lot of variations with different SCFs and FMSes were experimented with.

DFT calculations on the DOS of 3C-SiC were provided by SINTEF scientist Ole Martin Løvvik, and these calculations were assumed to be a good reflection of reality. Good agreement between DFT and Feff's *ldos* output files with respect to characteristic peaks and the band gap were achieved at SCF 10 and FMS 12. These values were therefore assumed to give the most accurate ELNES simulations, and the simulated 3C-SiC core loss spectra (ELNES spectra) presented in this report are based on input files with SCF 10, FMS 12. Figure 5.12 shows the good agreement between Feff and DFT in Si s-density of states at these values.
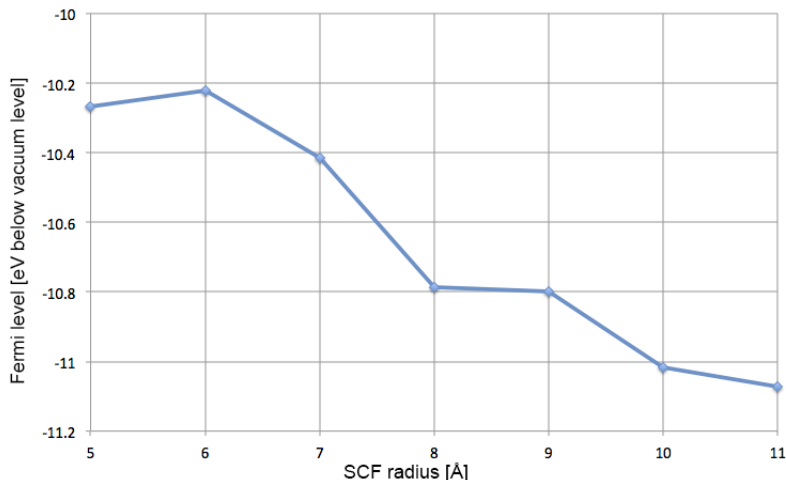
Figure 5.11: The Fermi level did not converge when increasing the SCF cluster radius.

The resulting edge simulations are in reasonable agreement with experimental spectra, as seen in Figure 5.13. A similar process was followed for 4H- and 6H-SiC.

It is worth noting that one should generate a large list of atoms from which to select a cluster (SCF and FMS values). It was found that if any parameter of radius approaching within one unit cell away from the outermost atom in the list, strange edge effects occur. So if one wishes to simulate 3C-SiC with FMS 12 Å, one needs a real space cartesian atom list in the input file of at least 17 Å in radius since a_{3C} is 4.36 Å. An atom list of 20 Å in radius was therefore used to be on the safe side in this thesis. The feff.inp input file for simulating the silicon L_2 edge in 3C-SiC is given in the appendix, Figure B.4.

5.7.2 Simulations of hexagonal SiC polytypes

It has been established that boron implantation and annealing generate stacking faults in the implanted region of 3C-SiC. Based on high resolution images, it is assumed that these stacking faults exhibit hexagonal SiC character. These local 4H/6H layers may affect the experimental ELNES spectra, distorting the effects from the actual boron. Pure 4H and 6H spectra were simulated in Feff in order to have a notion of whether this is a problem or not in experimental spectra. The polytype spectra are found in Figure 5.14 a). The spectra are quite similar, both the Si $L_{2,3}$ edges and the C K edges. Based on this, it is not expected that the stacking faults will affect the experimental ionisation edges sufficiently for detection. Both because of the fact that only a small fraction of the implanted material consists of hexagonal layers, and that the energy resolution obtained in experiments is 1.0 - 1.2 eV, which is too coarse for the small alterations between the polytypes.
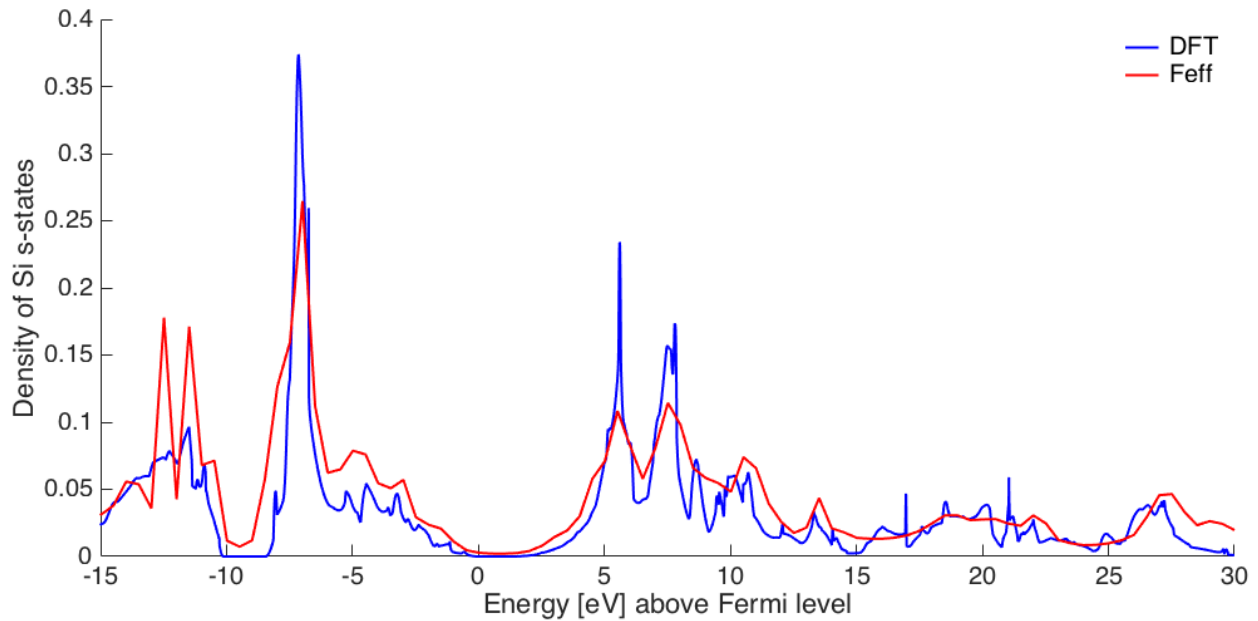
Figure 5.12: SCF 10 Å and FMS 12 Å provides good agreement between Feff's *ldos* output files and DFT calculations in the Si s-density of states for 3C-SiC.
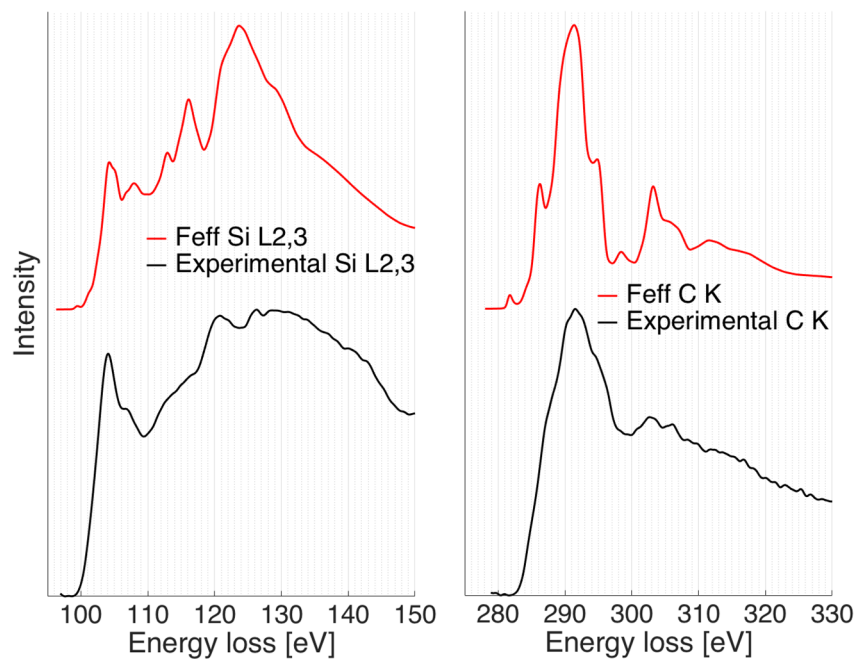
Figure 5.13: SCF 10 Å and FMS 12 Å provides decent agreement between simulated and experimental spectra in 3C-SiC. Simulations are lifted in intensity to be non-overlapping.
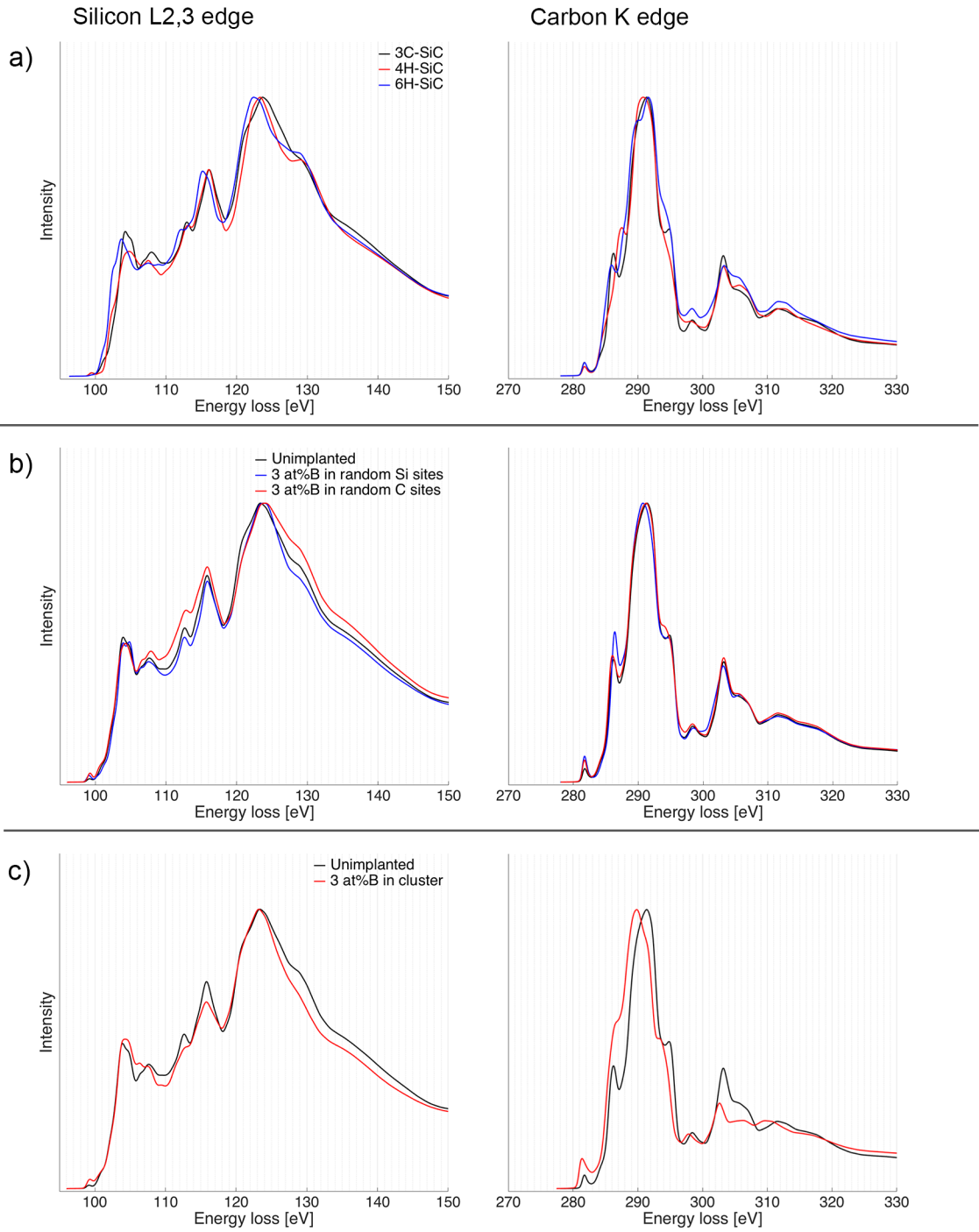
Figure 5.14: a) Simulated ionisation edges for unimplanted SiC polytypes. b) Simulated ionisation edges for substitutional boron in different lattice sites. c) Simulated ionisation edges for boron in cluster.

5.7.3 Simulations of substitutional boron

Matlab scripts for substitutional boron implantation of the atom list were written. The variations were:

- Substitutional 3 at% boron in random carbon lattice sites

- Substitutional 3 at% boron in random silicon lattice sites

The Matlab script for "implanting" boron in random silicon sites in the atom list is given in the appendix, Figure B.3. Since the scripts replace random silicon/carbon atoms, one might by chance get very few boron atoms close to the ionisation event in the simulation. The boron implantation scripts and corresponding simulations were therefore run multiple times to make sure randomness did not alter the results. The presented spectra from substitutionally boron implanted 3C-SiC, Figure 5.14 b), are based on random implantation distributions where proximity of boron atoms to the ionisation event were manually confirmed in the Feff input files. Based on these simulations, it seems unlikely that boron substitution will affect the Si $L_{2,3}$ and B K edges sufficiently so that the changes may be detected experimentally. Again, the alterations to the spectra are too fine for detection when working with an energy resolution of 1.0 - 1.2 eV. Recall also that most of the boron is likely found in the precipitate phase, and that the presented substitution simulations use 3 at% boron. Simulations with 2, and 1 at% boron were also performed, and it was unsurprisingly found that these spectra converge towards the unimplanted spectra when lowering the dose.

5.7.4 Simulations of boron cluster in 3C-SiC lattice

It has been argued that $B_{13}C_2$ is the likely precipitate phase. It would be a big challenge to write a script incorporating such a phase into the 3C-SiC structure in the feff.inp input file. A crude approximation to this was performed by writing a Matlab script for a pure boron particle in the 3C-SiC lattice. The spherical boron cluster of 95 atoms was placed spatially close (3 Å) to the ionisation event. The resulting simulated spectra are found in Figure 5.14 c). Again, it was found that the alterations to the spectra are very tiny. The silicon $L_{2,3}$ edge remains virtually unchanged, but there is however a shift in the peak position of 1.5 eV in the carbon K edge. This shift might be detectable experimentally, as the deviation is larger than the experimental energy resolution.

5.8 Experimental electron energy loss spectra

5.8.1 Experimental EELS: SiC polytypes

Sample 3-1 was made from a cross section "sandwich" with both 3C, 4H and 6H-SiC polytypes. This made it possible to test wether Feff simulations were correct in predicting the non-responsiveness of the ionisation edges to the polytypes. Figure 5.15 b) shows that the experimental spectra are in fact more similar than predicted by Feff. This is likely because of the coarse energy resolution in experiments, but it could also indicate a problem with the simulations. In any case, it seems that the hexagonal layers in the implanted material will not cause detectable changes in the ionisation edges.
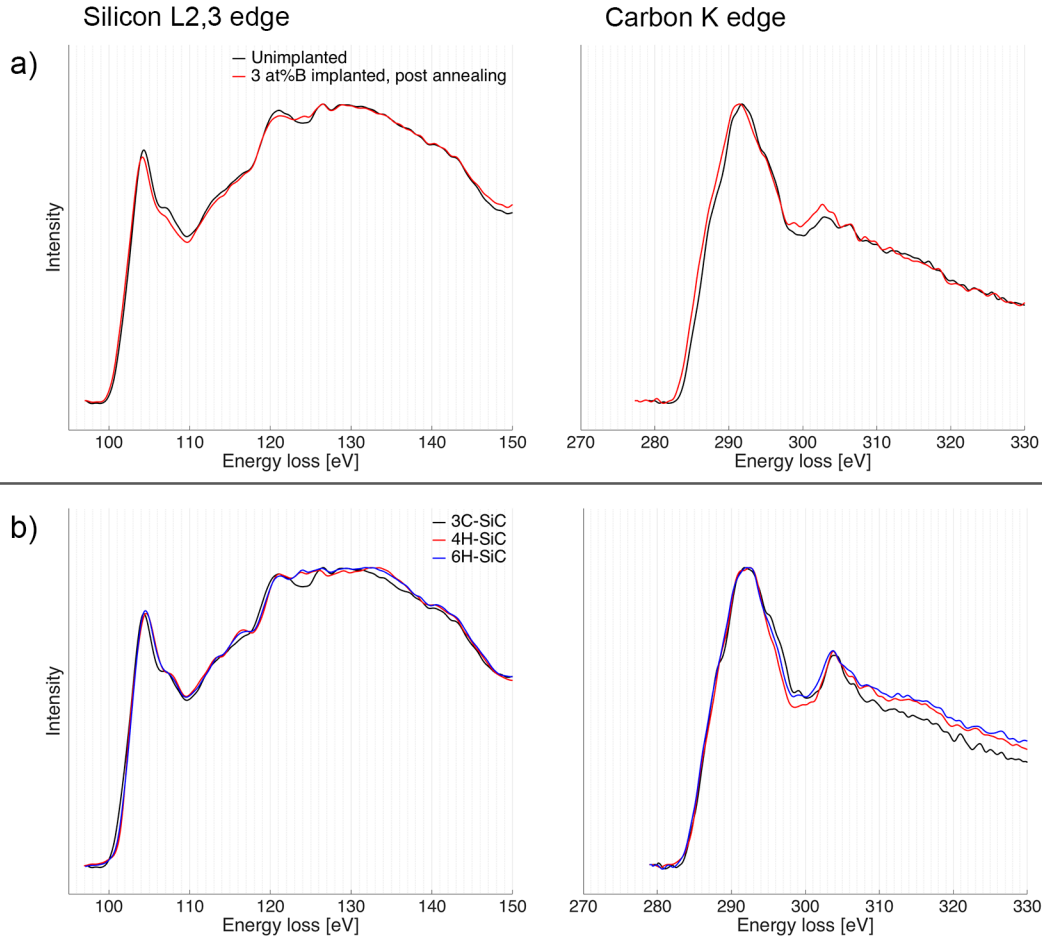
Figure 5.15: a) Experimental ionisation edges for implanted and unimplanted samples. b) Experimental ionisation edges for unimplanted SiC polytypes.

5.8.2 Experimental EELS: Implanted vs. non-implanted 3C-SiC

It has been established that boron-implanted, annealed 3C-SiC has precipitates, stacking faults, and probably some degree of atomic substitution. There are therefore a lot of individual factors which can cause alterations in experimental ELNES spectra. Feff simulations have however in general predicted very small individual alterations resulting from these factors. Sample 1-1 and 3-2 were used for data acquisition comparing unimplanted and implanted spectra in Figure 5.15 a). The two sets of spectra are even more similar than what is predicted by the simulations. The peak shift in the carbon K edge of 1.5 eV predicted by Feff on the basis of boron precipitates is not observed. The similarity of the two sets of spectra show that it is impossible to use the silicon and carbon ionisation edges to reveal the nature of the boron distribution in the lattice, especially with the available energy resolution. This is unfortunate, as objectives 4 and 5 are devoted to exactly this. Feff simulations were however successful in predicting the non-responsiveness to boron implantation in 3C-SiC.

Low loss spectra from implanted and pure samples were also compared to look for changes to the plasmon peak position. From Equation 4.6 one can calculate the theoretical peak position, assuming free valence electrons. If boron takes substitutional positions in the lattice, it is natural to assume that the valence electron density in the implanted material would be lowered since Si and C are group IV and B is group III. 3 at% substitutional boron corresponds to one boron atom per four unit cells of 3C-SiC, which means that the valence electron density would be 31.75 valence electrons per unit cell, as opposed to 32 for pure SiC. The corresponding calculated shift in plasmon peak position would in this case be 0.1 eV, as calculated from Equation 4.6. No statistically significant change in the plasmon peak position was found between implanted and pure EEL spectra. This supports the notion of a solid solubility of boron in 3C-SiC far less than 3 at%. A change of 0.1 eV can however easily go unnoticed when working with an energy dispersion of 0.1 eV per channel.

Chapter 6

Conclusions and further directions for *SunSiC*

This thesis was set out to investigate how boron implantation and subsequent annealing affects the atomic scale structure of 3C-SiC for solar cell applications, as part of the *SunSiC* project. Revealing the nature of the boron distribution in the 3C-SiC lattice has also been a main point of interest. Understanding the structural effects of the implantation and annealing procedures is important because solar cell materials must have high crystalline quality to be efficient. The investigation was done through transmission electron microscopy, using high resolution imaging, diffraction patterns, and electron energy loss spectroscopy experiments and simulations. The findings were presented and discussed in Chapter 5. This chapter will tie together the results, and give recommendations for further directions to the *SunSiC*-project.

It was found that the as-grown 3C-SiC crystals from LiU are almost defect-free, disregarding the macro scale domain phase boundaries. It has been shown that boron implantation of 2-3 at% performed at 400°C amorphises the 3C-SiC crystal structure, and that annealing for one hour at 1400°C gives complete epitaxial and single crystalline recrystallisation of the implanted layer. A significant increase in stacking faults concentration was found as a result of annealing, in addition to the formation of precipitates. The stacking faults seem to be related to a high boron concentration and not implantation damage, as the top boron-poor 100 nm in the implanted samples were found free of stacking faults. It has in this thesis been argued that the observed precipitates consist of the boron-rich phase $B_{13}C_2$, and that the formation of these, is a way for the likely supersaturated lattice to get rid of excess boron. On the basis of a small shrinkage of the lattice parameter with implantation, it was concluded that while most of the boron is likely found in the precipitates, some degree of atomic substitution also takes place. It was, based on diffraction data and DFT calculations, argued that the boron atoms likely take silicon lattice sites, and this hypothesis was tested further by use of EELS simulations and experiments. Nothing conclusive was however gained from using this approach, as both EELS simulations and experiments showed that boron implantation does not affect the energy loss spectra in a significant way. A method for simulating the silicon L edges and the carbon K edge was however developed with reliable results.

49

The work performed in this thesis suggests that the boron implantation dose of 2-3 at% probably is too high. If boron implanted 3C-SiC is to be used as a solar cell material, it is desirable to avoid both precipitates and stacking faults, as these very likely will increase carrier recombination, lowering the photovoltaic efficiency. Lowering the implantation dose while keeping the same implantation- and annealing temperature will probably lower the amount of precipitates formed during annealing. Lowering the implantation dose might also reduce the amount of stacking faults, as these were not found in recrystallised 3C-SiC regions containing 10^{19} - 10^{20} boron atoms/cm^3. The intermediate band has however been theorised to arise from high boron concentrations, so a lowering of the implantation dose may be counterproductive for solar cell applications. It has however been argued that increasing the temperature to 750 °C may counteract the amorphisation during implantation. If annealing can be avoided, one might achieve a boron super-saturated 3C-SiC lattice free of precipitates and possibly also free of stacking faults.

Appendix A

Abbreviations and symbols

A.1   Abbreviations

3C-SiC - Cubic silicon carbide

CB - Conduction band

CCD - Charge-coupled device

DOS - Density of states

DFT - Density functional theory

EDS - Energy-dispersive X-ray spectroscopy

EELS - Electron energy loss spectroscopy

EEL - Electron energy loss

ELNES - (Electron) energy loss near-edge structure

FIB - Focused ion beam

FMS - Full multiple scattering

HRTEM - High resolution transmission electron microscopy

IB - Intermediate band

IBSC - Intermediate band solar cell

ldos - Local density of states

LiU - University of Linköping

NTNU - Norwegian University of Science and Technology

SCF - Self consistent field

SRH - Shockley Read Hall (recombination)

TEM - Transmission electron microscope

PV - Photovoltaic(s)

VB - Valence band

VLM - Visible light microscope

ZA - Zone axis

ZLP - Zero loss peak

A.2 Symbols

$\mathbf{a_{3C,\ 4H,\ 6H}}$ - the lattice parameter of different SiC polytypes

$\mathbf{a_{3C,\ implanted}}$ - the lattice parameter of boron implanted 3C-SiC

$\mathbf{a_{3C,\ unimplanted}}$ - the lattice parameter of 3C-SiC

at% - atomic percent

$\mathbf{E_g}$ - band-gap

eV - electron volts

μm - micrometer - 10^{-6} meter

nm - nanometer 10^{-9} meter

Å - ångrström - 10^{-10} meter

pm - picometer 10^{-12} meter

Appendix B

Additional data

B.1   Band diagrams

This page is intentionally left blank for a full size band diagram figure on the next page.
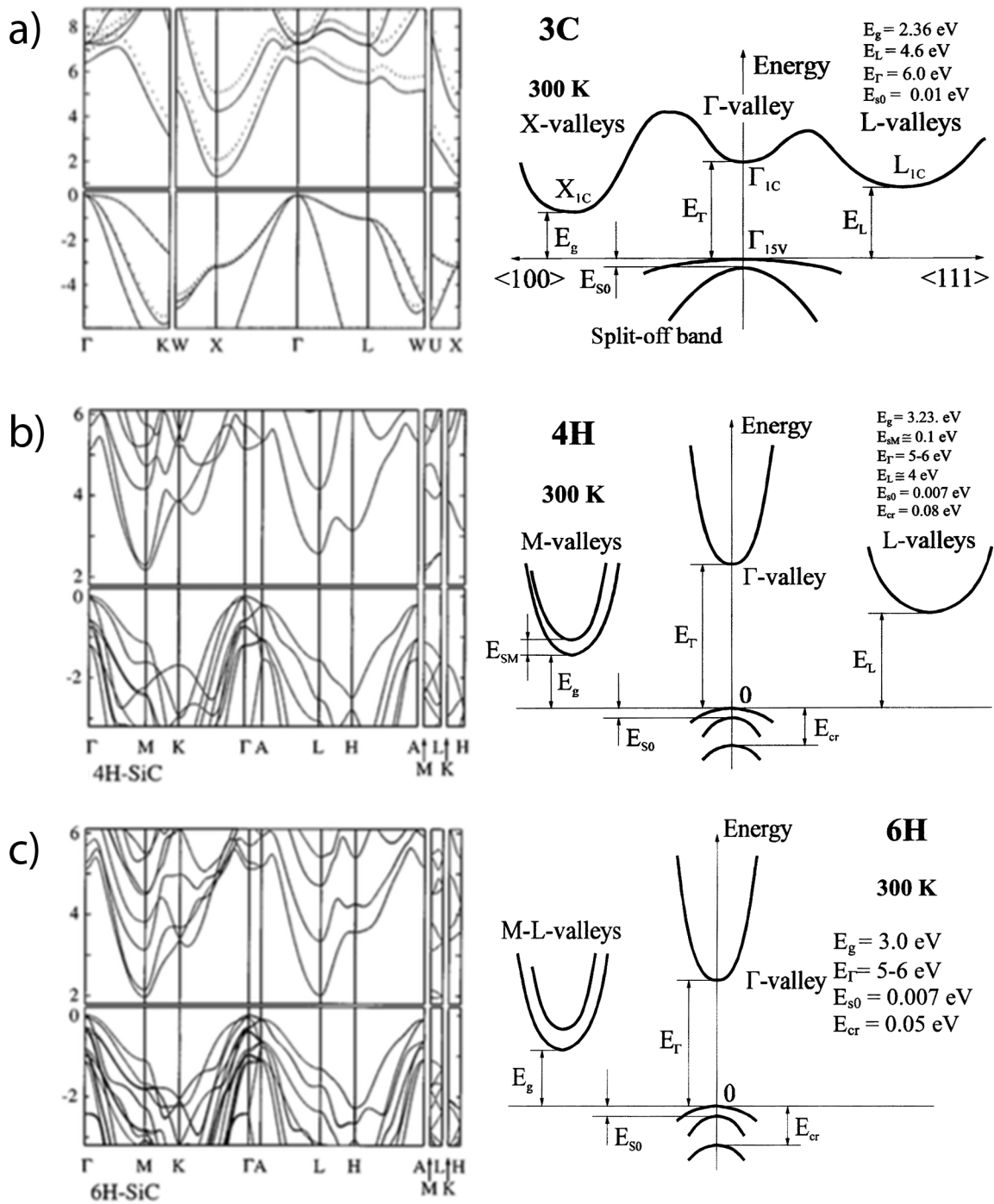
Figure B.1: Energy bands close to the band gap for a) 3C-SiC, b) 4H-SiC and c) 6H-SiC. Band diagrams are from reference [41]. The simplified band diagrams are based on [41], and are acquired from [53].

```
Interpolation_and_convolution.m  ✕  +
 1       %Creating a new energy axis
 2 -     minE = 97;
 3 -     maxE = 240;
 4 -     Enew=minE:0.05:maxE;
 5       %Combining the L2 and L3 edges using interpolation
 6 -     RND3BL2x = G(1,:);
 7 -     RND3BL2new = interp1(RND3BL2x,RND3BL2,Enew);
 8 -     RND3BL3x = H(1,:);
 9 -     RND3BL3new = interp1(RND3BL3x,RND3BL3,Enew);
10 -     RND3BL23 = RND3BL2new + RND3BL3new;
11       % Thanks to associate professor Øystein Prytz
12       % at UiO for help with the interpolation script
13
14
15
16       %Creating a gaussian for convolution
17 -     x=-5:0.1:5;
18 -     gauss = gaussmf(x, [0.51 0]);
19       %Convolution
20 -     RND3BL23conv = conv(RND3BL23,gauss, 'same');
21       % Thanks to PhD candidate Domas Birenis
22       % at UiO for help with the convolution script
23
```

Figure B.2: Matlab code for interpolation and convolution of Feff simulated silicon L_2 and L_3 spectra.

```
DopescriptByttSi.m    ×    +
 1 -      clc; clear all; close all;
 2
 3 -      fil1 = fopen('sil23.dat','r');
 4 -      [A] = fscanf(fil1,'%f',[6,inf]);
 5 -      atomliste = A(4,:);
 6 -      fclose(fil1);
 7
 8 -      dopingprosent = 0.03;
 9 -      atomer = length(atomliste);
10 -      dopingatomer = floor(atomer*dopingprosent);
11 -      dopingteller = 0;
12
13 -   ⊟ while dopingteller < dopingatomer
14 -          index = ceil(rand*atomer);
15 -          if atomliste(index) == 1
16 -              atomliste(index) = 3;
17 -              dopingteller = dopingteller + 1;
18 -          else
19 -              dopingteller = dopingteller;
20 -          end
21 -    └ end
22
23 -      atomliste = atomliste';
24 -      A = A';
25 -      A(:,4) = atomliste;
26
27 -      dlmwrite('dopedatomlist.dat',A,'delimiter','\t');
```

Figure B.3: The Matlab script written for substituting random silicon atoms by boron for the Si L_2 and L_3 ELNES simulations. The 4th column in A contains potentials, where potential 1 is silicon, 2 is carbon and 3 is boron. The input file sil23.dat is the atom list taken from the feff.inp file used to simulate pure 3C-SiC. This input file is given in Figure B.4.

```
TITLE 3C-SiC L2

*  Si L2 edge energy =  99.80 eV
EDGE       L2
S02        1.0

*          pot    xsph   fms    paths genfmt ff2chi
CONTROL    1      1      1      1      1      1
PRINT      1      0      0      0      0      0


                          *** ixc=0 means to use Hedin-Lundqvist
*          ixc  [ Vr  Vi ]
EXCHANGE   0

*          r_scf  [ l_scf   n_scf   ca ]
SCF        10.0


 COREHOLE FSR

ELNES 8.0 0.07 0.0
197 0 1 1
1 0 1
3 3
50 1
0.0 0.0


*          r_fms      l_fms
FMS         12  0


*          emin   emax   eimag
LDOS       -30    20     0.1


POTENTIALS
*    ipot   Z  element          l_scmt  l_fms   stoichiometry
       0   14   Si                  2      2      0.001
       1   14   Si                  2      2      4
       2    6   C                   1      1      4

ATOMS                         * this list contains 3193 atoms
*    x          y          z     ipot  tag           distance
   0.00000    0.00000    0.00000  0    Si            0.00000    0
   1.08990    1.08990    1.08990  2    C             1.88776    1
  -1.08990   -1.08990    1.08990  2    C             1.88776    2
  -1.08990    1.08990   -1.08990  2    C             1.88776    3
   1.08990   -1.08990   -1.08990  2    C             1.88776    4
   2.17980    2.17980    0.00000  1    Si            3.08270    5
  -2.17980    2.17980    0.00000  1    Si            3.08270    6
   2.17980   -2.17980    0.00000  1    Si            3.08270    7
  -2.17980   -2.17980    0.00000  1    Si            3.08270    8
```
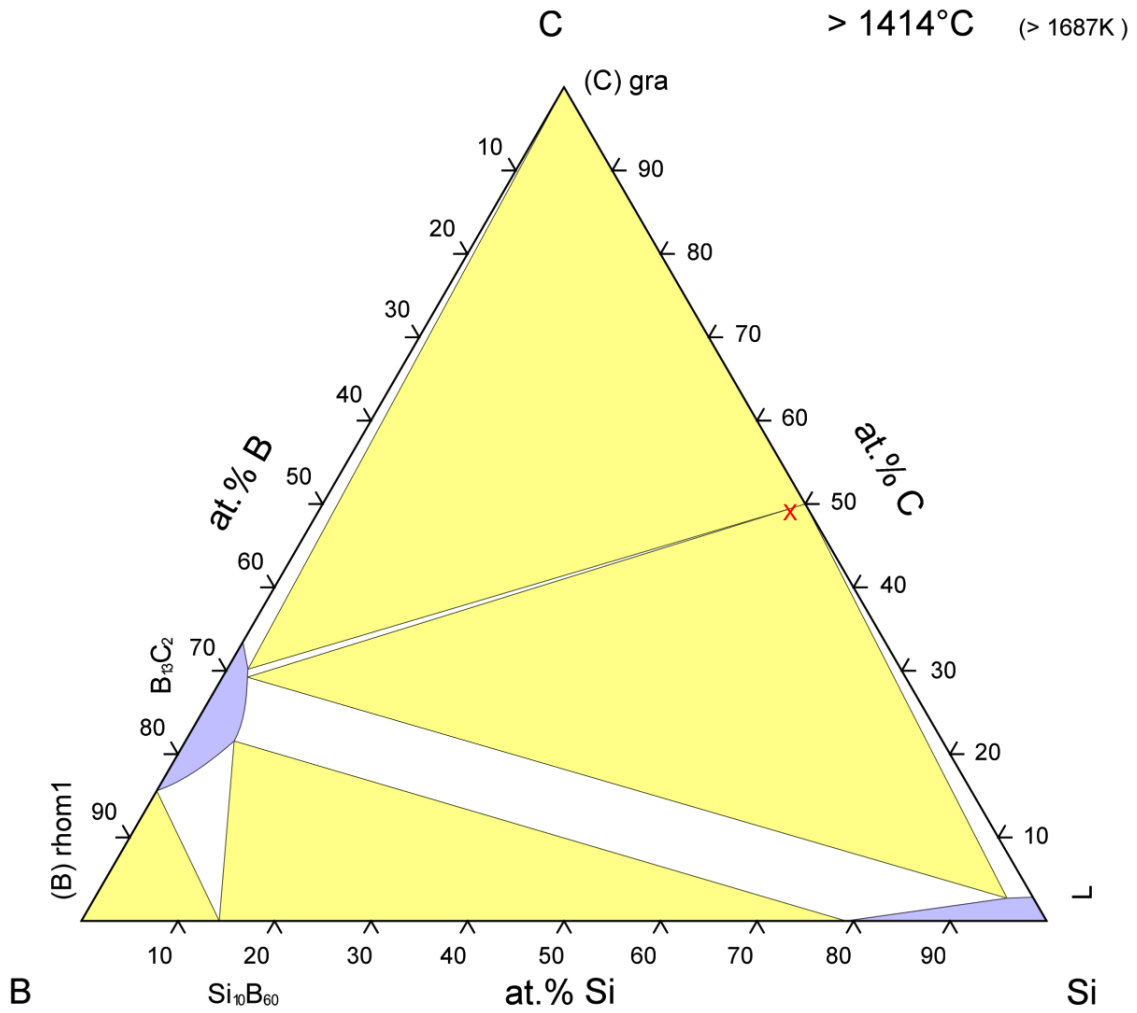
Figure B.4: The feff.inp file used for the silicon L_2 ELNES simulation in 3C-SiC. The "ATOMS" list consists of 3193 atoms, which corresponds to a 3C-SiC sphere of 20 Å radius.

Figure B.5: The ternary phase diagram for Si, C and B at 1414°C, diagram from [62].

Bibliography

[1] J. L. Sawin, "Renewables 2015: Global status report", tech. rep., *REN21*, 2015

[2] National Center for Photovoltaics, http://www.nrel.gov/ncpv/ Accessed 02.10.15

[3] J. Nelson, "The Physics of Solar Cells", *Imperial College Press*, 2003.

[4] Richter, et al. "Reassessment of the Limiting Efficiency for Crystalline Silicon Solar Cells". *IEEE Journal of Photovoltaics,* Vol 3, no 4, 2013

[5] V. Jokubavicius, M. Syväjärvi, et al. "Single domain 3C-SiC growth on off-oriented 4H-SiC substrates", *Crystal Growth and Design*, 15, pp 2940-2947, 2015

[6] Feff, a software for simulating EELS spectra. Version 9.6, official web page: http://feffproject.org Accessed 30.09.15

[7] A. Luque and A. Martí, "Increasing the efficiency of ideal solar cells by photon induced transitions at intermediate levels" *Physical Review Letters*, vol 78, no. 26, p. 5014-2017, 1997

[8] C. Kittel. "Introduction to Solid State Physics", *John Wiley and Sons inc.*, 8th edition, 2005.

[9] Al Luque and A. Martí, "The intermediate band solar cell: progress toward the realization of an attractive concept", *Advanced Materials*, 22, 160-174, 2010

[10] W. Shockley, W. T. Read, Jr. "Statistics of the recombinations of holes and electrons", *Physical Review*, 87, 5, 1952

[11] S. Bruun, O. Devik, "Fysikk for realgymnaset - elektrisitet", *Olaf Norlis Forlag Oslo*, 7th edition, 1956

[12] Australian Institute of Physics, web page: http://www.vicphysics.org/documents/events/stav2005/spe Accessed 25.11.15

[13] M. Yoshida, et al. "Photon ratchet intermediate band solar cells" *Appl. Phys. Lett. 100, 263902 (2012)*

[14] H. Heidarzadeth, et al. "Effect on conversion efficiency from dopants in SiC", *Springer Proceedings in Physics*, vol 155, pp 119-124, 2014

[15] A. Marti, L. Cuadra, A. Luque, "Partial filling of a quantum dot intermediate band for solar cells" *Electronic Devices*, vol 48, no. 10, pp. 2394-2399, 2001.

[16] Y. Okada, N. Ekins-Daukes, et al. "Intermediate band solar cells: Recent progress and future directions" *Applied Physics Reviews*, 2, 021302, 2015

[17] A Luque, A. Martí, E. Antonlín, C. Tablero, "Intermediate band versus levels in non-radiative recombination", *Physica B*, 382, 320-327, 2006

[18] R. Strandberg, *Theoretical studies of the intermediate band solar cell,* PhD thesis, 2010.

[19] P. Wahnon and C. Tablero, "Ab initio electronic structure calculations for metallic intermediate band formation in photovoltaic materials", *Physical Review B*, 65, 165115

[20] R. Lucena, I. Aguilera, et al. "Synthesis and Spectral Properties of Nanocrystalline V-Substituted In2S3, a Novel Material for More Efficient Use of Solar Radiation" *Chemistry of Materials*, 20, 5125-5127, 2008

[21] W. Wang, A. Lin, J. Phillips, "Intermediate-band photovoltaic solar cell based on ZnTe:O", *Applied Physics Letters*, 95, 011103, 2009

[22] E. Antolin, A Marti, et al. "Lifetime recovery in ultrahighly titanium-doped silicon for the implementation of an intermediate band material" *Applied Physics letters*, 94, 042115, 2009

[23] J. Kirch, B. Halperin and A. Aspuru-Guzik, "Nonradiative lifetimes in intermediate band photovoltaics - Absence of lifetime recovery", *Journal of Applied Physics*, 112, 013707, 2012

[24] T. H. DiStefano and J. J. Cuomo, "Reduction of grain boundary recombination in polycrystalline silicon solar cells", *Applied Physics Letters*, 30, 351, 1977

[25] B. Marsen, et al. "Investigation of the Sub-Bandgap Photoresponse inCuGaS2: Fe for Intermediate Band Solar Cells", *Progress in Photovoltaics*, 20, 625-629, 2011

[26] P. G. Linares, et al. "Extreme voltage recovery in GaAs:Ti intermediate band solar cells", *Solar Energy Materials and Solar Cells*, 108, 175-179, 2013

[27] J. Sheu, et al. "Photoresponses of manganese-doped gallium nitride grown by metalorganic vaporphase epitaxy", *Applied Physics Letters*, 102, 071107, 2013

[28] H. Kuwabara, et al. "Radiative recombination in beta-SiC doped with boron", *Journal of Luminescence*, 12/13, 531-536, 1976

[29] B. Richards, et al. "3C-SiC as a future photovoltaic material", *Conference: Photovoltaic Energy Conversion, 2003. Proceedings of 3rd World*

[30] V. Jokubavicius, et al. "Lateral enlargement growth mechanism of 3C-SiC on off-oriented 4H-SiC substrates", *Crystal Growth and Design*, 14, pp 6514-6520, 2014

[31] M. Syväjärvi, et al. "Cubic silicon carbide as a potential photovoltaic material", *Solar Energy Materials and Solar Cells*, http://dx.doi.org/10.1016/j.solmat.2015.08.029, 2015

[32] A. Martí, E. Antonlín, et al. "Production of Photocurrent due to Intermediate-to-Conduction-Band Transitions: A Demonstration of a Key Operating Principle of the Intermediate-Band Solar Cell", *Physical Review Letters*, 97, 247701, 2006

[33] E. G. Acheson, "Carborundum: Its history, manufacture and uses." *Journal of the Franklin Institue*, 136:279-289, 1893.

[34] D. N. Hume and I. M Kolthoff, "The silicon carbide electrode" *Journal of the American Chemical Society*, 63:2805-2806, 1941.

[35] J. B. Casady and R. W. Johnson, "Status of silicon carbide (SiC) as a wide-bandgap semiconductor for high-temperature applications: A review" *Solid-State Electronics* 39(10):1409-1422, 1996

[36] H. Ou, Y. Ou, et al. "Advances in wide bandgap SiC for optoelectronics" *Eur. Phys. J. B*, 87: 58, 2014

[37] G.R. Fisher and P. Barnes, "Toward a unified view of polytypism in siliocn carbide", *Phil. Mag. B*, vol. 61, pp. 217-236, 1990

[38] R. Vasiliauskas, et al. "Effect of initial substrate conditions on growth of cubic silicon carbide" *Journal of Crystal Growth*, 324, 7-14, 2011

[39] R. J. Iwanowski, K. Fronc, W. Paszkowicz, M. Heinonen, "XPS and XRD study of crystalline 3C-SiC grown by sublimation method", *Journal of Alloys and Compounds*, 286, p. 143-147, 1999

[40] V. Cimalla, et al. "Group III nitride and SiC based MEMS and NEMS: material properties, technology and applications" *J. Phys. D: Appl. Phys.*, 40, 6386-6434, 2007

[41] C. Persson, U. Lindefelt, "Relativistic band structure calculation of cubic and hexagonal SiC polytypes", *Journal of Applied Physics*, 82, 5496, 1997

[42] J. W. Sun, I. G Ivanov, et al. "Considerably long carrier lifetimes in high-quality 3C-SiC(111)", *Applied Physics Letters*, 100, 25, 252101, 2012

[43] P. Ivanov and V. E. Chelnokov, "Recent developments in SiC single-crystal electronics. *Semi-conductor Science and Technology*, 7, 863-880, 1999

[44] Y. M. Tairov, V. F. Tsvetkov, "Investigation of growth processes of ingots of silicon carbide single crystals", *Journal of Crystal Growth*, 43, 209-212, 1977

[45] J. Takahashi, N. Ohtani, M. Kanaya, "Structural defects in alpha-SiC single crystals grown by the modified-Lely method", *Journal of Crystal Growth*, 167, 596-606, 1996

[46] Murphy, Douglas, "Fundamentals of light microscopy and electron imaging", *Wiley-Liss*, 1st edition 2001. ISBN: 978-0-471-23429-6

[47] Williams, Carter, "Transmission electron microscopy", *Springer US*, 2nd edition 2009. ISBN: 978-0-387-76500-6

[48] Jeol, "Instructions JEM-2100F Field Emission Electron Microscope" user manual

[49] J. Solberg, V. Hansen, "Innføring i transmisjon elektronmikroskopi", compendium published by *NTNU*, 2014

[50] R. Brydson, "Electron energy loss spectroscopy", *BIOS Scientific Publishers Limited*, 2001

[51] University of Washington, "User's Guide, FEFF version 9.6.4"

[52] B. Ravel, Web Atoms version 1.8, http://cars9.uchicago.edu/cgi-bin/atoms/atoms.cgi, Accessed 03.12.15. Note that the website is down as of 19.04.16. The cause is unknown.

[53] Ioffe Institute, a Russian research institution, http://www.ioffe.ru/SVA/NSM/Semicond/SiC/bandstr. Accessed 27.11.15.

[54] H. Iwata, U. Lindefelt, et al. "Theoretical study of planar defects in silicon carbide", *Journal of Condensed Matter*, 12733–12740, 2002

[55] P. Käckell, J. Furthmüller and F. Bechstedt, "Stacking faults in group-IV crystals: An ab initio study" *Phys. Rev. B*, 1998

[56] S. Prussin, David I. Margolese, and Richard N. Tauber, "Formation of amorphous layers by ion implantation", *Journal of Applied Physics*, 57, 1985

[57] Carl J. McHargue, J. M Williams, "Ion implantation effects in silicon carbide", *Nuclear Instruments and Methods in Physics Research Section B*, 80-81, pp. 889-894, 1993

[58] Pearson's Crystal Data, a crystallographic database published by *ASM International*. http://www.crystalimpact.com/pcd/

[59] J. Lähnemann, U Jahn, et al. "Luminescence associated with stacking faults in GaN" *Journal of Applied Physics*, 47, 2014

[60] WebElements, a database on the periodic table by *The University of Sheffield*. www.webelements.com accessed 18.04.16

[61] William D. Callister, Jr. "Materials Science and Engineering", *John Wiley & Sons, Inc.*, 7th edition 2007. ISBN-13: 978-0-471-73696-7

[62] ASM Alloy Phase Diagram Database, *ASM International*, http://mio.asminternational.org/apd/index.aspx accessed 28.04.16

[63] Yo Tajima, W. D. Kingery, "Solid Solubility of Aluminum and Boron in Silicon Carbide", *Communications of the American Ceramic Society*, C27-29, 1982

[64] K. L. More, C. H Carter, et al, "Occurrence and Distribution of Boron-ContainingPhases in Sintered a-Silicon Carbide", *J. Am. Ceram. SOC*, 69, 695-98, 1986

[65] M. K. Linnarsson, M. S. Janson, et al, "Formation of precipitates in heavily boron doped 4H-SiC", *Applied Surface Science*, 252, 5316–5320, 2006

[66] EELS Data Base, the largest open-access electronic repository of spectra from EELS experiments, https://eelsdb.eu/spectra/, Accessed 09.12.15